Title
Compact Magnetic Shielding Using Thick-Film Electroplated Permalloy

Author
Wu, Jimmy

Publication Date
2020

UNIVERSITY OF CALIFORNIA

Los Angeles

Compact Magnetic Shielding Using Thick-Film Electroplated Permalloy

A dissertation submitted in partial satisfaction of the
requirements for the degree Doctor of Philosophy
in Electrical and Computer Engineering

by

Jimmy Chen-Yen Wu

2020

ABSTRACT OF THE DISSERTATION

Compact Magnetic Shielding Using Thick-Film Electroplated Permalloy

by

Jimmy Chen-Yen Wu
Doctor of Philosophy in Electrical and Computer Engineering
University of California, Los Angeles, 2020
Professor Robert N. Candler, Chair

Compact integration of clocks and inertial sensors using atomic, molecular, and optical (AMO) technology is necessary to create a self-contained navigation system resistant to external interference. However, the trend in miniaturization of AMO systems places the magnetic field of particle traps, optical isolators, and vacuum pumps close to other system components. Stray fields and field fluctuations cause changes in atomic transition frequencies, raising the noise floor and reducing the valuable stability in these precision devices. Therefore, it is critical to shield these magnetic fields away from sensitive subsystems by shunting them through low reluctance paths. This is accomplished with high permeability magnetic materials which either surround the precision components or the source of the magnetic field itself. Current magnetic shields are conventionally machined single or multi-layer structures made of various iron alloys. At smaller size scales, these manufacturing methods are ineffective at accommodating the various device and interconnect shapes, making multi-system integration challenging.

This work demonstrates batch fabricated high permeability magnetic shielding using permalloy electroplating techniques to simultaneously push the limits of minimum size, maximum shielding factor, and minimum cost. In particular, it presents the first experimental demonstration of electrodeposited high permeability, compact magnetic shielding at millimeter and sub-millimeter scales of fields exceeding 15 mT. Single layer shields of 300 µm permalloy with inner dimensions varying from 3 mm to 6.5 mm were fabricated on 3D printed polymer molds using a novel double-anode plating process to enable conformal deposition with uniform material properties. Multilayer shields of 10 µm permalloy and copper layers with inner dimensions of 1.5 mm to 6 mm were microfabricated using a bulk micromachining technique. The electroplated shields were designed with appropriate thickness to avoid saturation at the specified fields and with shapes to allow sophisticated interconnect extraction – a task that is challenging for conventional machining yet simple for microfabrication and electroplating. The size and shielding factor of these structures can enable compact integration of magnetic devices for AMO microsystems and other magnetic microelectronics, such as magnetic random-access memory and haptic actuators.

The dissertation of Jimmy Chen-Yen Wu is approved.

Sam Emaminejad

Chandrashekhar Joshi

Pietro Musumeci

Robert N. Candler, Committee Chair

University of California, Los Angeles

2020

TABLE OF CONTENTS

LIST OF FIGURES

LIST OF TABLES

ACKNOWLEDGEMENTS

I would like to thank Prof. Robert Candler for allowing me to pursue this dream of mine. Though this was not an easy path, he was always able to provide solid advice, both in research and in life, to keep me motivated. His genuine attitude towards his students is a quality that will follow me through my career.

Alongside Prof. Candler, all my current and former colleagues have kindly shared with me their assistance, advice, and companionship through my years at UCLA. Thank you to Dr. Jere Harrison, Dr. Yongha Hwang, Dr. Omeed Paydar, Dr. Jonathan Lake, Dr. Hyunmin Sohn, Dr. Srikanth Iyer, Dr. Yuan Dai, Dr. Max Ho, Dr. Sidhant Tiwari, Dr. Ling Li, Maggie Xiao, Siyuan Liu, Ben Pound, Erik Hodges, Nico Zani, Michaella Baltazar, Justin Shao, Sydney Walsh, and Hou Seng Wong.

I would also like to thank my committee members, Prof. Sam Emaminejad, Prof. Chandrashekhar Joshi, and Prof. Pietro Musumeci, for their feedback and comments to guide this dissertation to completion.

This work would not have been possible without the help of the staff members and facilities of the UCLA Nanoelectronics Research Facility, the Integrated Systems Nanofabrication Cleanroom, the Center for High Frequency Electronics, the Molecular & Nano Archaeologoy Laboratory, and the Bouchard Lab.

Finally, I want to give my gratitude to my family and friends who have never stopped supporting me through the tumultuous road to this degree. I hope I have made you all proud.

VITA

2011	Assistant Engineering Intern UC Berkeley Electronics Support Group Berkeley, California
2012-2013	Undergraduate Research Assistant Berkeley Computer Aided Manufacturing Berkeley, California
2013	Bachelor of Science in Electrical Engineering and Computer Sciences University of California, Berkeley Berkeley, California
2013-2019	Teaching Assistant and Graduate Student Researcher University of California, Los Angeles Los Angeles, California
2015	Master of Science in Electrical Engineering University of California, Los Angeles Los Angeles, California
2019-2020	Ph.D. Candidate University of California, Los Angeles Los Angeles, California

PUBLICATIONS AND PRESENTATIONS

J. Harrison, J. Wu, O. Paydar, Y. Hwang, E. Threkleld, J. Rosenzweig, P. Musumeci, R. Candler, “High-Gradient MEMS Electromagnets for Particle Beam Manipulation,” Proceedings of Solid State Sensors, Actuators, and Microsystems Workshop (Hilton Head), 2014.

J. Harrison, O. H. Paydar, Y. Hwang, J. Wu, E. Threlkeld, J. Rosenzweig, P. Musumeci, R. N. Candler, “Fabrication Process for thick film micromachined multi-pole electromagnets”, JMEMS Letter, Vol. 23, No. 3, 2014.

J. Harrison, Y. Hwang, O. Paydar, J. Wu, E. Threlkeld, J. Rosenzweig, P. Musumeci, R. N. Candler, “High-gradient microelectromechanical system quadrupole electromagnets for particle beam focusing and steering,” Phys. Rev. ST Accel. Beams 18, 023501, 2015.

I. Gadjev, R. Candler, C. Emma, J. Harrison, A. Nause, J. Wu, A. Gover, and J. Rosenzweig. "High-Gain, Short Wavelength FEL in the Raman Regime." Nuclear Instruments and Methods in Physics Research Section A: Accelerators, Spectrometers, Detectors and Associated Equipment, 2016.

J. C. Wu, L. Li, J. Harrison, R. Candler, “Micro- to millimeter scale magnetic shielding,” Solid-State Sensors, Actuators and Microsystems (Transducers), 2017.

R. N. Cander, J. C. Wu, L. Li, J. C. Harrison, “Multilayer Batch Microfabricated Magnetic Shielding”, Patent Application Submitted, 2019.

Chapter 1: Introduction

Section 1.1: What is Magnetic Shielding?

Originating from the relative motion of electric charges, including the constant movement of atomic charges found in all matter, magnetic fields literally surround the world. Humanity's most primitive tool for navigation, the compass, follows the Earth's own magnetic field (25 – 65 μT) generated by convection currents of molten iron in the outer core [1]. While this signal has historically been easy to trace, the introduction of electronic devices which use magnetic fields, such as vacuum tubes, transformers, and cell phones, has added significant magnetic noise in the background. On the other hand, many of these devices inherently require magnetically clean environments to operate and must be isolated from each other. Furthermore, recent technology relies on the measurement of various atomic signals, which are extremely sensitive to magnetic fields including the ever-present field of Earth. Thus, the increasing prevalence of magnetic devices has led to the development of magnetic shielding, which is meant to reduce the magnitude of a magnetic field in space.

Shielding of magnetic fields can be approached in two ways depending on the frequency of the noise. High frequency fields ($f \geq 1$ MHz) are electromagnetic waves and can be absorbed by a conductive material (e.g. copper, aluminum, etc.). This method uses the existence of electric monopoles to cancel the waves via image charges. However, for low frequency fields ($f < 1$ MHz), electricity and magnetism are decoupled thereby necessitating a different approach. Thus, magnetostatic fields are instead redirected with magnetic materials (e.g. nickel, iron, etc.). This is accomplished either by surrounding a magnetically sensitive device with a shield from an external magnetic field or by containing the source of undesired field itself within a shield to prevent it from leaking out.

Section 1.2: Applications of Magnetic Shielding

Magnetic shielding is necessary in applications where a device cannot operate in the presence of a magnetic field or where measurements cannot be interfered by an uncontrolled or undesired field. Various commercial applications already implement magnetic shielding in order to maintain the quality or precision of the product. Conventional cathode ray tube (CRT) based equipment, such as monitors, utilize deflecting magnetic coils to control the trajectory of an electron beam incident on a phosphor screen. Magnetic shields must be used to prevent Earth's magnetic field or stray fields from nearby equipment, such as speakers, from distorting the image. Furthermore, it is well known that mechanical watches fail at accurate time-keeping in the presence of strong magnetic fields due to the ferrous nature of the material used in the springs [2]. This has led popular brands like Rolex to develop magnetically shielded watches that can perform even in environments such as the European Organization for Nuclear Research (CERN), where quadrupoles and undulators in particle beamlines create fields on the order of 1 T. More recently, magnetoresistive random access memory (MRAM) is being investigated as a next-generation memory technology which uses electron spin instead of charge to store memory. Due to the compact packing nature of memory bits, it is necessary to prevent crosstalk and interference between each MRAM device using magnetic shielding [3].

On the other hand, at the forefront of scientific discoveries, there are several measurements which must be performed in environments with either well-controlled magnetic fields or in the absence of magnetic fields. One example is electric dipole moment (EDM) experiments where researchers are measuring the distribution of positive and negative charges inside neutrons in an attempt to find a permanent EDM. These measurements are systemically affected by a geometric phase effect related to the field gradient of the applied magnetic field [4]. Furthermore, while electroencephalography (EEG) has traditionally been a common technique to measure voltage fluctuations in the brain, the signal is often distorted by the conduction properties of the scalp, brain, and skull [5]. Recent studies have used an alternative, magnetoencephalography (MEG), to measure magnetic neural signals noninvasively using superconducting quantum interference devices (SQUID). However, detection of these biological magnetic signals requires field sensitivity less than 1 pT/$\sqrt{\mathrm{Hz}}$. Thus, magnetic shielding is necessary for various new measurement paradigms in order to shield away field noise and enable extremely accurate and precise sampling of the desired signals.

Finally, recent advances in atomic, molecular, and optical (AMO) devices using atomic traps and atomic interferometry have led to chip scale atomic clocks making high precision, atomic-based timing and navigation devices more accessible. However, further miniaturization is limited by stray magnetic fields from other nearby systems. As the magnetic shields discussed in this dissertation are largely motivated by these exciting new opportunities, the following section is dedicated to an in-depth introduction to atomic clocks and the potential applications and challenges on the road to miniaturization.

Section 1.3: Introduction to Atomic Clocks

In all timing applications, the most important parameter is precision, or the measure of how repeatable a measurement can be. One of the most consistent values that can be measured is the hyperfine transition frequency between two energy levels of an atom. In fact, the international unit of a second is defined as the duration it takes a cesium-133 atom to undergo 9,192,631,770 oscillations at a rest temperature of 0 K [6]. Thus, while people rely on quartz crystals or silicon resonators as timing elements in their wrist watches and electronics, accurate timekeeping is maintained by periodically syncing to a national standard. This standard is kept constant with an atomic clock to an error of only 10 nanoseconds per year.

Figure 1.1 shows the schematic diagram for a clock calibration circuit. A local oscillator provides the base timing reference, serving as the clock output. This oscillator also drives a microwave synthesizer, which then applies the generated microwaves to a physics package – the heart of all atomic clock systems. By calibrating this synthesized microwave frequency to the atomic transition frequency of atoms, an error is measured in the local oscillator frequency. This error signal is then given to a control loop which periodically tunes the local oscillator. Thus, the clock accuracy is ultimately determined by the stability of the physics package. Using this control scheme, the first atomic clock was demonstrated in 1949 at the National Institute of Standards and Technology (NIST) by calibrating a quartz crystal to the molecular vibration frequency of ammonia molecules [7]. While groundbreaking, it was nevertheless less accurate than the quartz standard at the time.

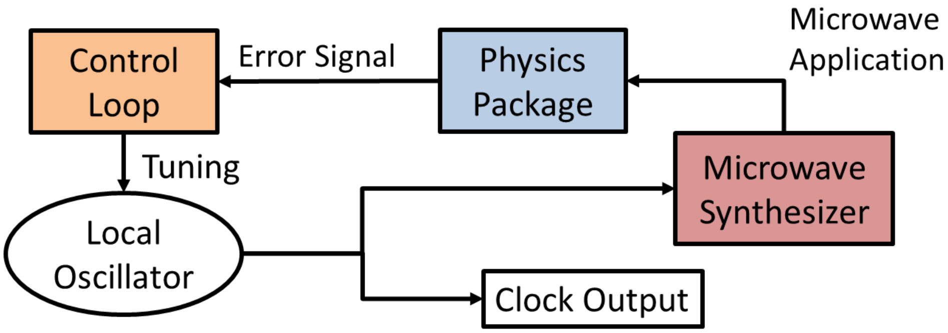

Figure 1.1: Feedback diagram of an atomic clock starting with the local oscillator feeding to a microwave synthesizer. The output from the physics package based on the microwave synthesizer helps the control loop to adjust the oscillator for precision timing.

Since then, similar methods have been applied to measure the hyperfine transition frequencies of cesium-133 and rubidium-87, which are the transitions currently used in modern atomic clocks [8]. Figure 1.2 details the working principles within a cesium-based physics package. Cesium-133 atoms are heated and collimated into a beam, which passes through an inhomogeneous magnetic field [9]. Due to the magnetic field gradient, particles with different magnetic spin moments are deflected in separate trajectories, allowing the magnets to act as a spin state selector. Next, the atoms pass through a uniform magnetic field that establishes a quantization axis. The microwave field synthesized from the local oscillator output is then applied to the cesium beam. After a brief drift length, it is applied again, causing the atoms to fully switch their spin states if the microwave frequency matches the cesium transition frequency. Finally, a second pair of asymmetric magnets splits the beam again, sending the transitioned cesium atoms to a detector. Thus, the output signal is related to the number of transitioned atoms, thereby acting as a measure of the local oscillator accuracy.

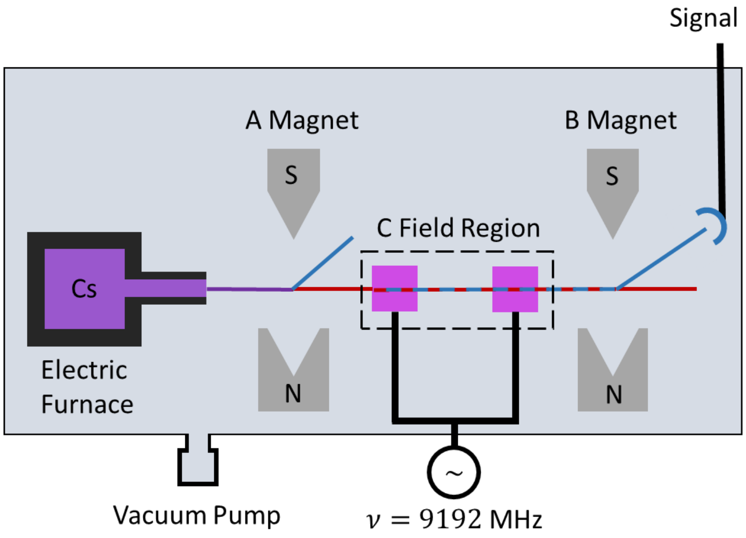

Figure 1.2: Diagram of a conventional cesium beam atomic clock. The output signal is correlated to the number of cesium atoms with transitioned states, which depends on the exactness of the applied microwave signal to the transition frequency.

While clocks based on the aforementioned cesium standard were previously used by NIST to set the national time standard, new optical atomic clocks reference their oscillators to transition frequencies in the optical range, improving the time resolution of the clocks by nearly five orders of magnitude [10]. Previously, atomic clocks were limited to countable microwave frequencies, as calibrating to even higher frequencies seemed impossible. However, the introduction of optical frequency combs, which divide optical frequencies down to lower countable microwave or radio signals, has enabled a new paradigm. The local oscillators in newer optical atomic clocks use a laser that is resonant with the atomic transition, and the correction signal is then derived from atomic spectroscopy. While extremely promising for further pushing the boundaries of time resolution and stability, these clocks are largely still an ongoing topic of research that is being improved on annually.

On the other hand, the most prevalent modern atomic clocks are based on rubidium physics packages. These clocks utilize a conceptually similar system to the cesium standard but replace the furnace and atom detector with a discharge lamp and photodiode [8]. As the light passes through a rubidium vapor cell, it is absorbed based on the spin state of the rubidium atoms. Thus, the output signal is the number of detected photons at the photodiode, which is dependent on the accuracy of a microwave synthesizer transitioning the rubidium atoms and changing the optical transmission of the vapor cell. Ultimately, rubidium-based atomic clocks provide an inexpensive and compact alternative where time-keeping accuracy can be traded for a smaller-sized package.

Section 1.2.1: Applications of Precision Timing

The various levels of time and measurement precision provided by the different types of atomic clocks are attractive for not only scientific verification and deep-space measurements but also more practical applications such as security network encryption and global or local positioning systems. As atomic clocks are extremely stable and therefore able to repeatedly reproduce the same measurement, small deviations away from the expected result can be traced to specific changes instead of noise. Thus, scientists are taking advantage of this to test our physical models and verify fundamental constants. One example is the fine structure constant, α, which characterizes the strength of electromagnetic interactions between elementary charged particles. Astrophysicists have measured the light from quasars generated ten billion years ago, claiming a variation in the fine structure constant from then to now [10]. By reproducing this same experiment but with only a year's difference in time, scientists have verified that there is no noticeable change in the tick speed of atomic clocks caused by this variation in the fine structure constant, effectively ruling out the findings from the astrophysical measurements.

However, the accuracy provided by atomic clocks can be utilized not only to measure temporal variations but also spatial variations. Einstein has shown through general relativity that time dilation occurs where gravity fields are stronger. Thus, atomic clocks will tick more slowly when closer to the center of the Earth than further away, where gravity is weaker. It is then possible to scan and map out the exact geometric surface of the Earth, a field called geodesy, by using the discrepancy in time reported by an optical atomic clock [11]. Figure 1.3 shows a demonstration of using atomic clocks for geodesy [12]. However, these systems are currently limited to laboratory environments where tables with precision-aligned optics enable the necessary resolution in time measurement. This makes implementation of these measurements challenging, as the tool is not portable enough to enable the universal geodetic mapping that scientists are pursuing.

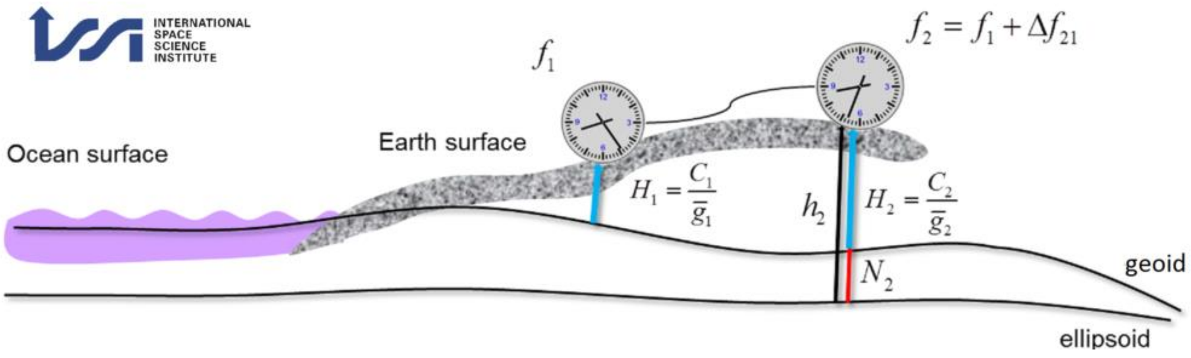

Figure 1.3: Example calculation of geodesy using atomic clocks. The frequency of the same electromagnetic signal is measured at locations 1 and 2 with height H_1 and H_2. The frequency shift, which can be accurately quantified with an atomic clock, will be dependent on the geopotential number C divided by the gravity g at each location [12].

Stepping down to applications that require less extreme precision, atomic clocks are most commonly used nowadays in positioning and navigation. Global Position System (GPS), the most prevalent method for position triangulation, is a radionavigation system consisting of over thirty satellites that are constantly transmitting signals containing the satellite's 3D position and time. In order to triangulate the client's position, each receiver synchronizes itself to the signal from four of these satellites. By using its own oscillator to determine delay, the receiver can then calculate the time-of-flight from each satellite in order to find four unknown parameters: its own 3D position and clock deviation. The accuracy of this position calculation is extremely reliant on the precision of this time delay as the signal travels at the speed of light: 1 μs of delay can result in over 300 m of position error. Thus, in order to achieve this level of accuracy, atomic clocks are loaded on each satellite, and ground monitoring stations are periodically calibrated to ensure these clocks stay accurate. Figure 1.4 shows a diagram of the working principle of GPS.

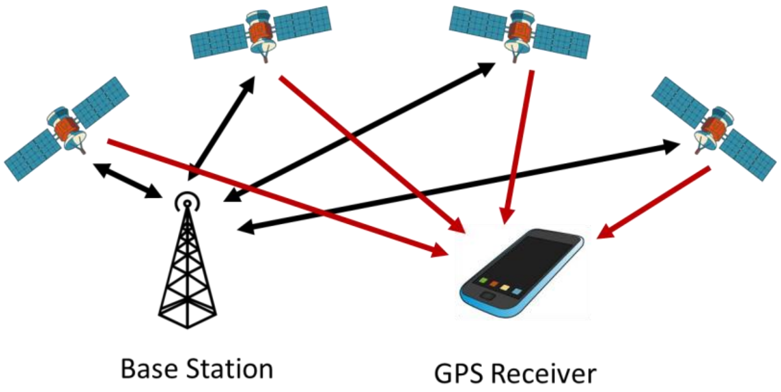

Figure 1.4: Illustration of GPS satellites synchronizing their local atomic clocks with the more precise clock of a base station. GPS receivers estimate their local position with time-of-flight using position signals from the satellites and a local quartz oscillator.

However, while GPS is critical to institutions such as the military to gain strategic advantages over the opposition, radio signals can easily be jammed on hostile territory. To a lesser extent, even constantly keeping track of signals from four satellites can be difficult for a GPS receiver in a commercial vehicle, causing the position to drift over time. Typically, the local timing in receivers is driven by a quartz oscillator, which, while reasonably accurate and cheap to manufacture, must periodically estimate its own error in order to calibrate properly to the atomic clocks in the GPS satellites. By replacing the quartz oscillator with an atomic clock in the receiver itself, several improvements can make the navigation system more resilient to noise or jamming mitigation [13]. Firstly, the synchronicity of the clock between the satellite and receiver can inherently improve the tracking time and signal-to-noise ratio of positioning determination. Furthermore, if the connection to satellite signals is interrupted, a local atomic clock can even continue to estimate its current position with fewer than four satellites in combination with local inertial sensors.

Section 1.2.2: Challenges of Miniaturization

While considerably smaller than a nearly ten cubic meter cesium fountain clock or state-of-the-art optical clocks, commercial rubidium oscillators still have a volume of several hundred cubic centimeters making them too large to integrate on the scale of a personal device. While commercial chip-scale atomic clocks are available, they trade off their accuracy and stability for decreased size, weight, and power consumption. Table 1.1 shows a comparison of various atomic clock technologies and the relevant applications at their size-scales [9][14][15]. Figure 1.5 shows the Allan deviation, a measure of frequency stability in clocks, reflecting the accuracy over time for the various timing systems in location positioning systems [13].

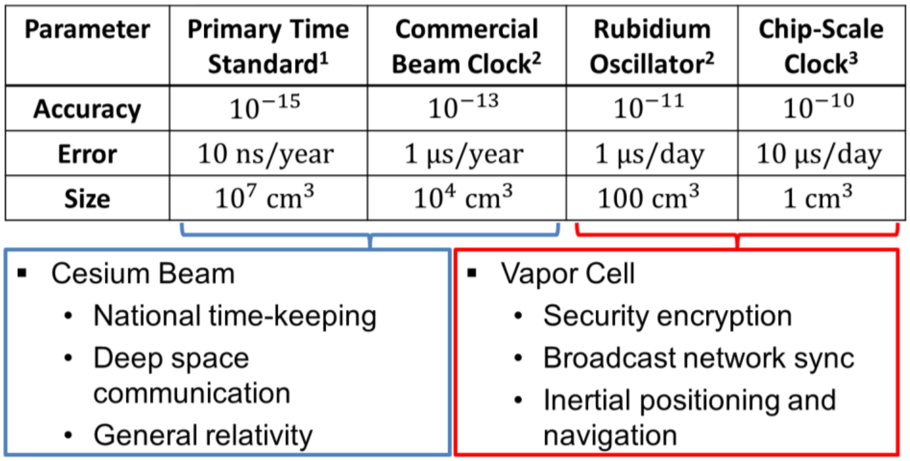

Parameter	Primary Time Standard[1]	Commercial Beam Clock[2]	Rubidium Oscillator[2]	Chip-Scale Clock[3]
Accuracy	10^{-15}	10^{-13}	10^{-11}	10^{-10}
Error	10 ns/year	1 μs/year	1 μs/day	10 μs/day
Size	10^7 cm^3	10^4 cm^3	100 cm^3	1 cm^3

- Cesium Beam
  - National time-keeping
  - Deep space communication
  - General relativity

- Vapor Cell
  - Security encryption
  - Broadcast network sync
  - Inertial positioning and navigation

Table 1.1: Comparisons of miniaturizing atomic clocks. Traditional and accurate cesium beam atomic clocks are used for national timekeeping or deep space communication. Rubidium oscillators provide an alternative to using vapor cells, offering less accurate readings at a smaller size scale for encryption or broadcast network timing. Chip-scale atomic clocks are currently being researched to provide high-precision, atomic-based timing for navigation and measurements. [9][14][15]

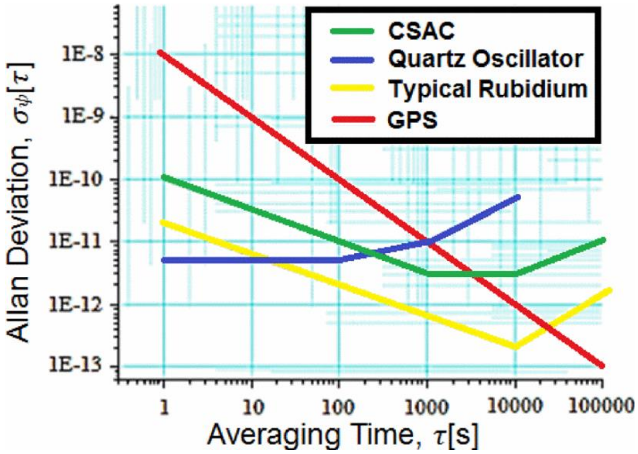

Figure 1.5: Comparison of the Allan Deviation over averaging time for GPS clocks, rubidium oscillators, quartz oscillators, and chip-scale atomic clocks [13].

Thus, a truly high-performance chip-scale atomic clock capable of proliferating to the level of individual users has yet to be developed. Further miniaturization of atomic clocks is inhibited by the various sources of instability that can be introduced. The total time error for the physics package of an atomic clock is given as follows:

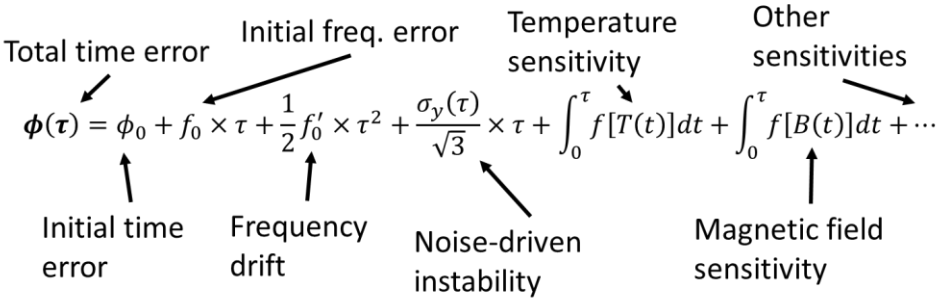

$$\boldsymbol{\phi}(\boldsymbol{\tau}) = \phi_0 + f_0 \times \tau + \frac{1}{2} f_0' \times \tau^2 + \frac{\sigma_y(\tau)}{\sqrt{3}} \times \tau + \int_0^\tau f[T(t)]dt + \int_0^\tau f[B(t)]dt + \cdots$$

The initial time and frequency errors are present from the start of calibration. However, over time, various sources introduce further drift in the frequency response itself caused by spectral broadening of the atomic transition. Changes to the temperature in the system can affect not only the atomic responses, but also the microwave synthesizers and detectors. While these various sources of error are present in all atomic clocks, the system's sensitivity to magnetic fields in particular becomes a challenge with further miniaturization. There are several sources of magnetic fields in these physics packages, such as the C Field for setting the quantization axis, optical isolators for laser-pumped rubidium, magneto-optical traps for cooling and stabilizing atoms, or Penning cell arrays for vacuum pumps. Each subsystem requires its own well-controlled field to operate and is sensitive to stray microTesla to milliTesa-scale fields from each other. Bringing them physically closer to each other in a smaller package introduces challenges to magnetic field isolation, which is achieved via low frequency magnetic shielding. While conventional atomic clocks also use some degree of shielding, realizing chip-scale clocks introduces a barrier of its own as magnetic shielding becomes challenging to implement at millimeter size-scales. Thus, by applying microfabrication techniques involving thick film, high permeability material, it is possible to achieve magnetic shielding at the sizes relevant to chip-scale atomic clocks.

Chapter 2: Magnetic Shielding Theory

Section 2.1: Electromagnetic Shielding

As both high and low frequency magnetic shielding relate to the interaction between matter and electromagnetic waves, the theory of shielding can be derived from Maxwell's equations. Assuming a periodic time dependence of $e^{j\omega t}$, Maxwell's equations in phasor form can be written as:

$$\nabla \times \vec{E} = -j\omega\vec{B} \tag{2.1}$$

$$\nabla \times \vec{H} = j\omega\vec{D} + \vec{J} \tag{2.2}$$

$$\nabla \cdot \vec{D} = \rho \tag{2.3}$$

$$\nabla \cdot \vec{B} = 0 \tag{2.4}$$

where $\vec{E}$ is the electric field, $\vec{H}$ is the magnetic field, $\vec{D}$ is the electric flux density, $\vec{B}$ is the magnetic flux density, $\vec{J}$ is the electric current density, ρ is the electric charge density, and ω is radial frequency. If the wave is traveling through a lossy medium with conductivity σ and permeability μ, then the curl equations can be rewritten as:

$$\nabla \times \vec{E} = -j\omega\mu\vec{H} \tag{2.5}$$

$$\nabla \times \vec{H} = j\omega\epsilon\vec{E} + \sigma\vec{E}. \tag{2.6}$$

These equations can be combined to create a wave equation for an electromagnetic wave traveling through the medium. The solution for such a wave traveling in the z-direction and polarized in the x-direction can be written as [16]:

$$E_x(z) = E^+e^{-\gamma z} + E^-e^{\gamma z} \tag{2.7}$$

where γ is the complex propagation constant with real part α and imaginary part β. From the wave equation, γ is defined as:

$$\gamma = \alpha + j\beta = j\omega\sqrt{\mu\epsilon}\sqrt{1 - \frac{j\sigma}{\omega\epsilon}}. \tag{2.8}$$

For a good conductor, it can be assumed that $\sigma \gg \omega\epsilon$, allowing α to be approximated as:

$$\alpha = \sqrt{\frac{\omega\mu\sigma}{2}} = \frac{1}{\delta_s} \tag{2.9}$$

where δ_s is defined as the skin depth of a conductor. The value α describes the exponential decaying term in the propagation of the wave through the lossy medium, where it is expected to decay by an amount $1/e$ after traveling one skin depth. This skin depth decreases with increasing frequency, permeability, and conductivity of the material. Thus, for a high frequency electromagnetic wave, shielding can be achieved simply by surrounding the area of interest using a conductive material such as copper or aluminum. Based on Maxwell's equations, the material generates eddy currents to oppose the influx of electromagnetic fields, nullifying and repelling the fields within.

Section 2.2: Low Frequency Magnetic Shielding

While conventional EMI shielding simply requires a conductor for shielding by image charges, low frequency magnetic shielding requires high permeability material to provide a low reluctance path, redirecting magnetic fields around its volume. Figure 2.1 shows a COMSOL Multiphysics simulation of a magnetic field passing through a non-magnetic cylinder and a cylinder of high permeability material. The magnetic fields are attracted to the magnetic material surrounding the shielded device as it is more energetically favorable, reshaping the field to avoid penetrating the volume and affecting device operation. Conventional magnetic shields typically use mumetal, a ferromagnetic alloy consisting of primarily nickel and iron, which can achieve relative permeabilities up to 100,000. These metals are relatively ductile and can be formed into thin sheets and rolled into the appropriate shape for the required magnetic shield.

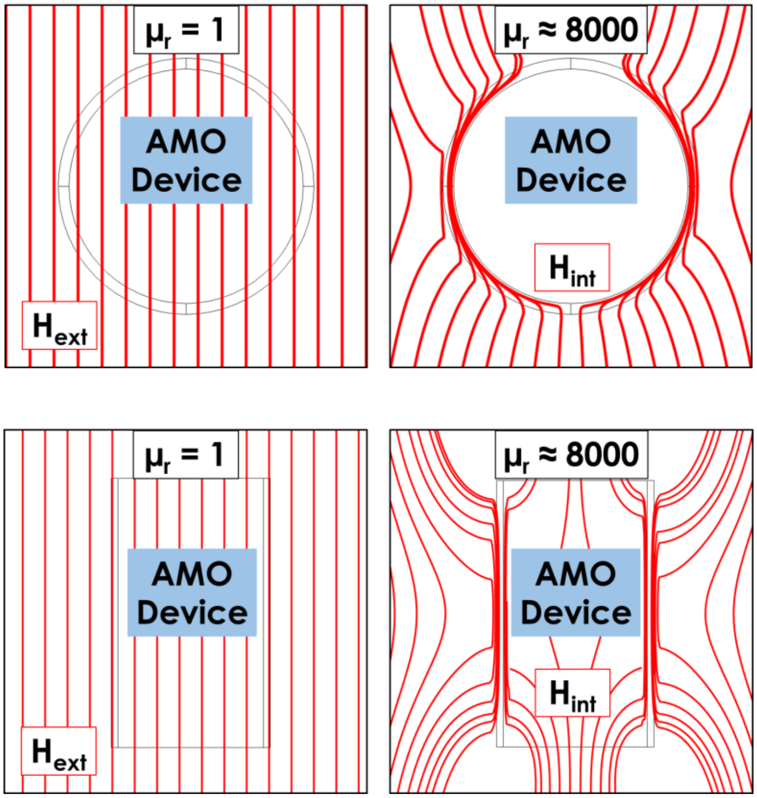

Figure 2.1: Simulation of an 11 mT field applied to a 300 μm thick non-magnetic (left) and magnetic permalloy (right) shell in the transverse (upper) and longitudinal (lower) directions. In the transverse case, fields are strongly redirected by the circular low reluctance path. In the longitudinal case, due to the lack of lips and less smooth reluctance, some fields manage to leak through, worsening shielding performance.

The effectiveness of shielding is characterized by the shielding factor, which is defined as:

$$S = \frac{H_{ext}}{H_{int}} \tag{2.10}$$

for the situation where a device, surrounded by a field H_{int}, is placed within a shield to protect it from an external field H_{ext}. In order to solve analytically for the shielding factor, it is necessary to refer back to Maxwell's equations. In the case of no free currents, Ampere's law can be written:

$$\nabla \times \vec{H} = 0 \tag{2.11}$$

which allows the definition of a magnetic potential W as:

$$\vec{H} = -\nabla W. \tag{2.12}$$

From Gauss's law for magnetism, we can then show that for a constant permeability μ:

$$\nabla^2 W = 0. \tag{2.13}$$

This is Laplace's equation for magnetic potential. Thus, to obtain the shielding factor S of a magnetic shield, one must solve the Laplacian for the magnetic potential while applying the proper boundary conditions for the desired geometry. For the case of a single spherical shell, the exact shielding factor is solved to be [17]:

$$S = 1 + \frac{2}{9}\frac{(\mu_r - 1)^2}{\mu_r}\left(1 - \frac{R_2^3}{R_1^3}\right) \tag{2.14}$$

where μ is the relative permeability, R_2 is the inner radius of the sphere, and R_1 is the outer radius of the sphere. Typically, $\mu_r \gg 1$ for shielding materials, and the total shield thickness $t \ll D$, the shield diameter, which simplifies the equation to:

$$S = \frac{4}{3}\frac{\mu_r t}{D}. \tag{2.15}$$

While the solution is analytically simple for a sphere, most practical shields are created in cylindrical shapes due to ease of fabrication. However, a simple analytical expression can only be derived for the unrealistic case of an infinitely long cylinder. Specifically, the magnetic field would be applied in the direction perpendicular to the axis of the cylinder, which yields the transverse shielding factor. By again applying the relevant boundary conditions to solve for the magnetic potential, this expression can be solved to be:

$$S = 1 + \frac{1}{4}\frac{(\mu_r - 1)^2}{\mu_r}\left(1 - \frac{r_2^2}{r_1^2}\right) \tag{2.16}$$

where r_2 is the inner radius of the cylinder, and r_1 is the outer radius of the cylinder. Applying the same assumptions as for the spherical shield, the equation can be simplified to:

$$S = \frac{\mu_r t}{D}. \tag{2.17}$$

Looking at the simplified equations for a spherical and cylindrical shield, it is evident that the fundamental scaling laws for single shell shielding factors are nearly identical with geometric sizes. While exact, closed form solutions of the shielding factors of a finite cylinder are not available, various approximations have been made for the transverse and longitudinal shielding factors, where the field is applied along the cylinder axis [17][18]. These estimations assume the shield can be approximated with an ellipsoid with a major and minor axis corresponding to the length and diameter of the cylinder. The geometry inherently lends itself to a smaller shielding factor in the longitudinal than transverse direction, even up to a factor of 10 [19].

However, by applying the same assumptions as with thin-shelled spheres and infinite cylinders, it is possible to obtain similar scaling laws for these shielding factors as well. Figure 2.2 demonstrates these scaling laws for the transverse shielding factor of an infinite cylinder. From initial inspection, it can be concluded that higher shielding factors can be obtained with higher permeability or thicker shields. However, the former is a property of the material used, which is difficult to exceed 10^5 without the use of external active biasing [20]. On the other hand, the potential thickness of the shield is tied to the maximum size of the shielding layer, which is limited by the application. Thus, in order to obtain even higher shielding factors, it is necessary to construct shields consisting of multiple layers.

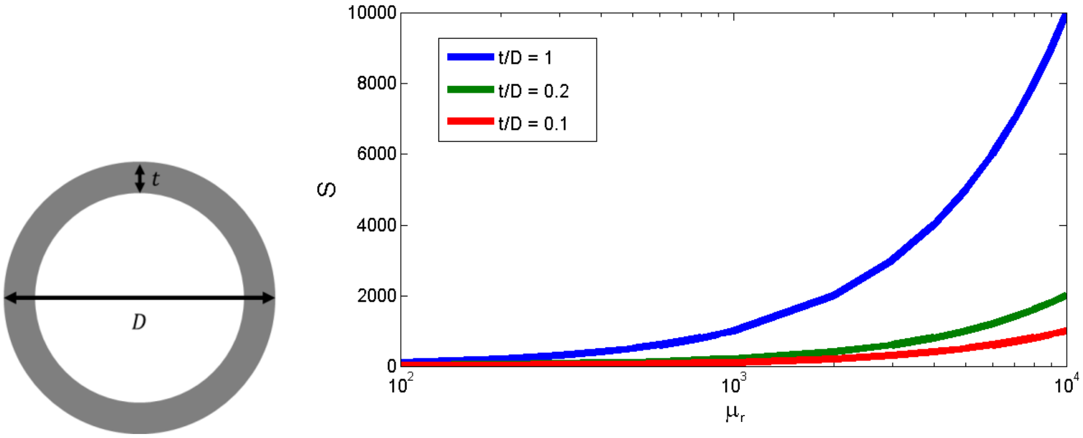

Figure 2.2: Plot of the shielding factor for a cylindrical shell in the transverse direction with varying thickness to diameter ratios.

Section 2.3: Multilayer Magnetic Shielding

In order to understand the benefit of a multi-layer shield compared to a single layer shield, it is essential to conceptually examine the method by which shielding affects the magnetic field lines of its surroundings. Figure 2.3 shows a simulation of a magnetic field being applied in the transverse direction to a thinner 300 μm cylindrical shield and a thicker 1.5 mm cylindrical shield having the same outer diameter both with $\mu_r = 8500$. While the shielding factor is higher for the thicker shield, which is to be expected based on the single layer scaling equations, the magnetic flux lines indicate a different conclusion about efficiency. In the case of the thicker shell, flux lines are drawn into the high permeability material and tend to follow the curvature of the shell instead of penetrating into the shield. It can be seen that the flux lines closer to the inner surface of the shell are redirected a greater distance, implying that the inner surface is more effective at shielding than the outer surface. This observation is even more pronounced in the case of the thinner shell. By reducing the thickness of the shell while keeping the outer radius the same, the inner surface is effectively pushed closer to the outer surface, making greater use of its strength in bending the flux lines. Thus, it can be inferred that by adding several individual layers of thinner shells totaling the same shielding thickness, a higher shielding factor can be achieved as adding several inner shielding surfaces maximizes the efficiency of the material.

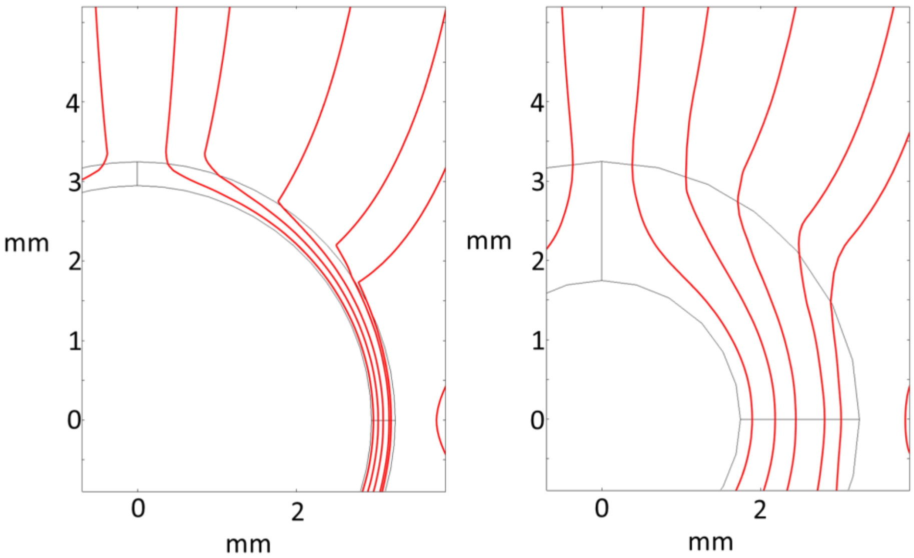

Figure 2.3: Simulation of a 15 mT field applied in the transverse direction to a 300 µm shell (left) and 1.5 mm shell (right) both with outer diameter 3.3 mm.

Section 2.3.1: Multilayer Shielding Equation

The same conclusion can be drawn by deriving the multilayer shielding factor equation using Maxwell’s equations [21]. Consider the n-layer transverse cylindrical shield depicted in Figure 2.4. To find the magnetic field in each region, it is necessary to apply Laplace’s equation with the appropriate boundary conditions to solve for the magnetic scalar potential W.

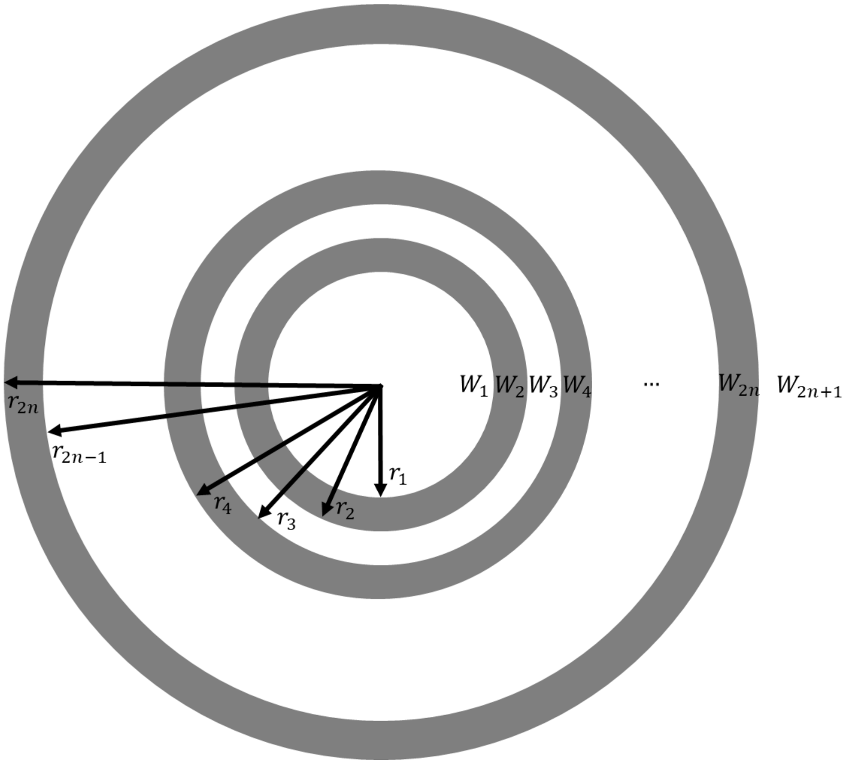

Figure 2.4: Diagram of an n-layer transverse cylindrical shield with each consecutive boundary having inner radius r and magnetic scalar potential W as labeled.

In cylindrical coordinates (ρ, θ, z), the general solution for magnetic potential in the k-th region can be written as:

$$W_k = \left(C_k \rho + \frac{D_k}{\rho}\right) \cos(\theta). \tag{2.18}$$

where C_k and D_k are unknown constants that must be solved with the boundary conditions of the problem. Maxwell's equations dictate that the normal component of the magnetic flux density $\vec{B}$ and the tangential component of the magnetic field $\vec{H}$ must be continuous across boundaries. Therefore, by taking the gradient of W in cylindrical coordinates, the magnetostatic boundary conditions can be written as:

$$\mu_k \frac{dW_k}{d\rho}\bigg|_{r_k} = \mu_{k+1} \frac{dW_{k+1}}{d\rho}\bigg|_{r_k} \tag{2.18}$$

$$\frac{1}{r_k}\frac{dW_k}{d\theta}\bigg|_{r_k} = \frac{1}{r_k}\frac{dW_{k+1}}{d\theta}\bigg|_{r_k}. \tag{2.19}$$

For the potential to remain finite at the center of the shield, $D_1 = 0$, so the flux density in the center region is written as:

$$\vec{B}_1 = -\mu_0 C_1\big(\cos(\theta) \cdot \hat{\boldsymbol{\rho}} - \sin(\theta) \cdot \hat{\boldsymbol{\theta}}\big), \tag{2.20}$$

where μ_0 is the vacuum permeability and $\hat{\boldsymbol{\rho}}$ and $\hat{\boldsymbol{\theta}}$ are the unit vectors in the corresponding cylindrical coordinate direction. This is a uniform field of magnitude $\mu_0 C_1$. Outside of the shield, the flux density can be written as:

$$\vec{B}_{2n+1} = -\mu_0(C_{2n+1} - D_{2n+1}/\rho^2)\cos(\theta) \cdot \hat{\boldsymbol{\rho}} + \mu_0(C_{2n+1} + D_{2n+1}/\rho^2)\sin(\theta) \cdot \hat{\boldsymbol{\theta}}. \tag{2.21}$$

Taken far away from the cylinder, this equation simplifies to:

$$\vec{B}_0 = -\mu_0 C_{2n+1}\big(\cos(\theta) \cdot \hat{\boldsymbol{\rho}} - \sin(\theta) \cdot \hat{\boldsymbol{\theta}}\big), \tag{2.22}$$

which is again a uniform field, but of magnitude $\mu_0 C_{2n+1}$. Thus, the shielding factor can be derived by taking the quotient of the external field by the internal field, which is:

$$S = \frac{\vec{B}_0}{\vec{B}_1} = \frac{C_{2n+1}}{C_1}. \tag{2.23}$$

By applying the boundary conditions directly to the equation of magnetic potential in each k-th region, the following recursion relations can be found for odd k:

$$C_{k+1} = \frac{1}{2}\left[C_k\left(1+\frac{1}{\mu_m}\right)+\frac{D_k}{r_k}\left(1-\frac{1}{\mu_m}\right)\right] \tag{2.24}$$

$$D_{k+1} = \frac{1}{2}\left[C_k r_k^2\left(1-\frac{1}{\mu_m}\right)+D_k\left(1+\frac{1}{\mu_m}\right)\right] \tag{2.25}$$

where the index $m = (k+1)/2$ is introduced such that μ_m refers to the relative permeability of the m-th layer of shielding. From here, once again, by applying the conditions of $\mu_m \gg 1$ and $t \gg D$, we can simplify the recursion relations into:

$$C_{k+2} = C_k\left(1+\frac{\mu_m t_m}{2R_m}\right)+D_k\left(\frac{\mu_m t_m}{2R_m^3}\right) \tag{2.26}$$

$$D_{k+2} = -C_k\left(\frac{\mu_m t_m R_m}{2}\right)+D_k\left(1-\frac{\mu_m t_m}{2R_m}\right). \tag{2.27}$$

Using these equations, the transverse shielding factor for an infinite cylinder is then shown to be:

$$S = C_3 = \frac{\mu_{r1} t_1}{D_1}, \tag{2.28}$$

which matches the previously derived equation.

For a general concentric cylindrical shield with n layers, the total shielding factor can be written as a sum of polynomials [22]:

$$S = \sum_{k=0}^{n} P_k \tag{2.29}$$

$$P_1 = \sum_{i=1}^{n} S_i = S_1 + S_2 + \cdots + S_n \tag{2.30}$$

$$P_0 = 1 \tag{2.31}$$

$$P_2 = \sum_{i=1}^{n-1}\sum_{j>i}^{n} S_i d_{i,j} S_j = S_1 d_{1,2} S_2 + S_1 d_{1,3} S_3 + \cdots + S_2 d_{2,3} S_3 + \cdots + S_{n-1} d_{n-1,n} \tag{2.32}$$

$$P_{n-1} = S_1 d_{1,2} S_2 d_{2,3} \dots S_{n-2} d_{n-2,n-1} S_{n-1} + \cdots + S_2 d_{2,3} S_3 d_{3,4} \dots S_{n-1} d_{n-1,n} S_n \tag{2.33}$$

$$P_n = S_1 d_{1,2} S_2 d_{23} \dots S_{n-1} d_{n-1,n} S_n \tag{2.34}$$

$$d_{i,j} = 1 - \frac{D_i^2}{D_j^2} \tag{2.35}$$

where d_{ij} is the normalized difference in cross-sectional area between consecutive shields while indexing outwards. The first polynomial P_1 is the intuitive sum of the individual shielding factors, but the higher order polynomials show that the total shielding factor scales multiplicatively with the number of layers, provided that the individual shielding factors are high when compared to their associated d_{ij} parameters. Simply put, a large number of thin shields can provide a much higher shielding factor than a single shield with the same total material thickness.

Section 2.3.2: Multilayer Shielding Trends

By replacing the thicker conventionally rolled mumetal layers with thinner electroplated permalloy layers, much higher shielding factors can potentially be obtained. Figure 2.5 demonstrates the scaling of MEMS-scale multilayer permalloy shields compared to Metglas or other mumetals using the shielding factor equation above. A vast increase in shielding factor by several orders of magnitude is predicted by increasing the number of shields within a constant total thickness. Shielding factor gain begins to level off with increasing total shield thickness. This is because individual shielding factors start degrading significantly with more layers as the shields are too weak given the inner diameter. This effect is further evident in Figure 2.6. By decreasing the inner shield diameter, thinner shields achieve massive gains in shielding factor due to the multiplicative inverse dependence.

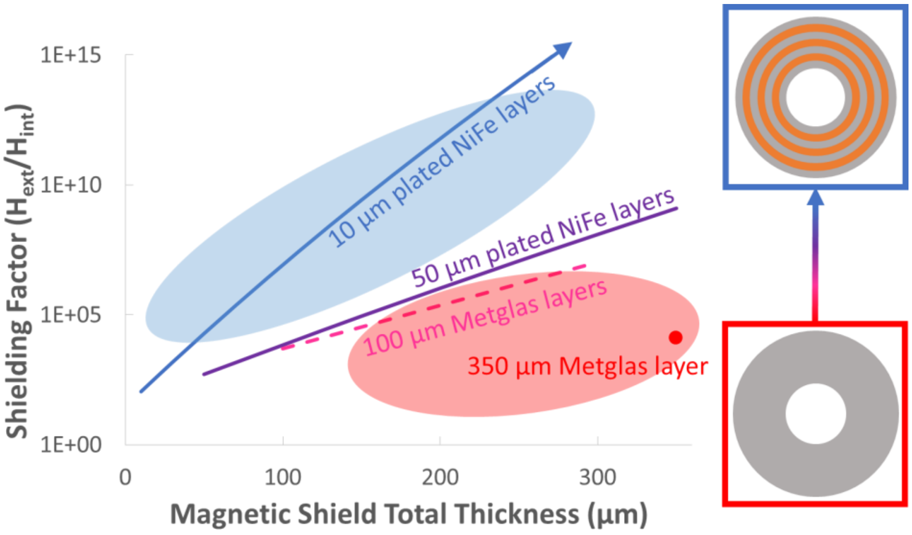

Figure 2.5: Plot of analytical shielding factor as a function of total magnetic shield thickness for spherical shields with a 1 mm inner diameter. The blue region shows multilayer, electroplated nickel-iron shields, and the red region shows conventionally machined Metglas shields.

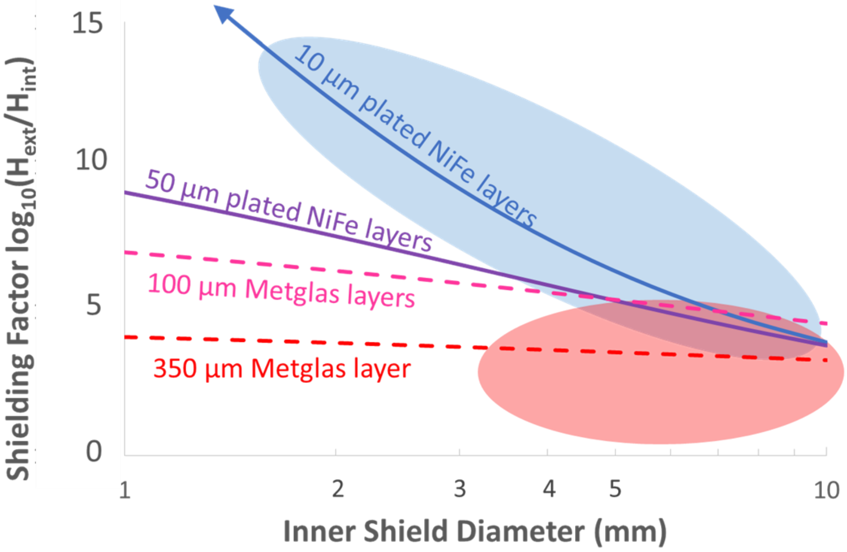

Figure 2.6: Plot of analytical shielding factor as a function of inner shield diameter for spherical shields with a total shield thickness of 350 μm. The blue region shows multilayer, electroplated nickel-iron shields, and the red region shows the current size of conventionally machined Metglas shields.

Optimal shielding factor can be attained by tailoring the thickness and spacing of thin shield layers for a given field to operate at the edge of saturation, providing the highest shielding factor with the most compact shield. This process is challenging for conventional machining yet relatively simple using the batch fabrication methods demonstrated in MEMS processes. From the analytical perspective, it is evident that optimizations of shield thickness to the appropriate characteristic lengths can enable microfabricated permalloy shields to demonstrate unprecedented levels of magnetic shielding.

Section 2.4: Magnetic Saturation

However, while multilayer shielding can be extremely beneficial for the appropriate dimensions, it is critical to consider the behavior of magnetic materials in the presence of increasingly stronger fields. To understand this, it is necessary to review the fundamental magnetization process of materials. Inherently, the spin of unpaired electrons in atomic or molecular electron orbitals generates a permanent magnetic moment. Furthermore, the movement of electrons orbiting around a nucleus creates an atomic magnetic moment, similar to the magnetic field moment of a current loop [23]. In a paramagnetic material, these individual moments weakly interact with each other, so with no externally applied field, they are randomly oriented. As seen in Figure 2.7a, there is no net magnetization in the sample. While an externally applied field increases in magnitude, the moments start to align towards the field as in Figure 2.7b, resulting in a linear increase in the net magnetization. This alignment is still weak, however, as the thermal energy wanting to randomly orient the moments is still large relative to the magnetic energy. For example, with an applied field $H = 10^5$ A/m, the magnetization of water would only be $B \approx 0.125$ T.

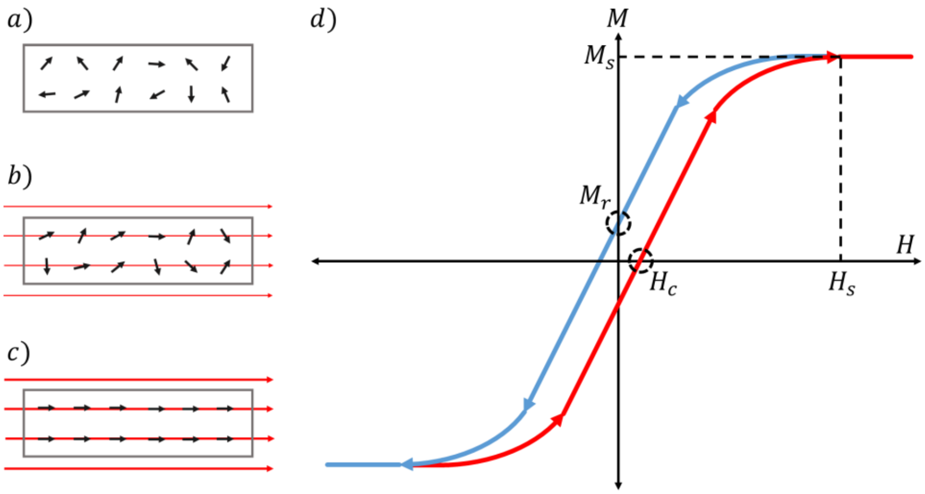

Figure 2.7: Diagram of moments in a paramagnetic material aligning with increasing applied external biasing field (a, b, c). Plot showing the magnetization behavior of a ferromagnetic material (d) exhibiting hysteresis with different magnetization routes taken by an increasingly positive field (red) and negative field (blue).

However, the magnetic moments in ferromagnetic materials behave differently, strongly interacting with each other even in the absence of an external magnetic field. These moments tend to form together in magnetic domains, which are regions in which large, internal fields align the moments within them in parallel. Thus, when applying an external field, the domain walls start to shift, increasing the size of the domains which are aligned with the field. Since this domain energy is much greater than that of thermal energy, ferromagnets, such as permalloy, can achieve higher magnetization ($B \approx 1$ T) with lower applied fields ($H \approx 100$ A/m). As the applied field continues to increase, the domain walls eventually disappear. This means the sample has fully magnetized at its saturation magnetization M_s as in Figure 2.7c.

Figure 2.7d shows the $M - H$ curve of a ferromagnetic material. As mentioned above, the magnetization of the sample increases with applied field, asymptotically approaching M_s. The slope of this curve is the magnetic susceptibility χ, from which the relative permeability of the material is defined as $\mu_r = 1 + \chi$. The magnitude of field required to practically saturate the material is the saturation field H_s. As a consequence of saturation, the material permeability decreases as the applied field increases, eventually reaching $\mu_r = 1$ at H_s. Thus, an ideal shielding material has a high M_s, retaining a large μ_r for shielding over a greater range of externally applied field.

It can be also observed that the curve exhibits hysteresis, which can be explained by the magnetic remanence M_r. After fully saturating a sample, decreasing the applied field does not fully revert the internal magnetization, leaving a magnetic remanence M_r at zero external field. This is because domain wall motion is an inherently lossy process, meaning it is more energetically favorable for the sample to remain slightly magnetized. In order to demagnetize the sample in that direction, it is necessary to apply a coercive field H_c in the opposite direction. To fully demagnetize the sample, the applied field must be alternatively swept in the positive and negative directions with decreasing magnitude. This process is known as “degaussing” the sample.

A material with large H_c is denoted as “hard”, while a low H_c results in a “soft” material. High remanence can be a desirable trait of neodymium (NdFeB), which is meant to be a hard, permanent magnet that is difficult to demagnetize. However, for magnetic shielding, it is necessary to use materials with low remanence and coercivity such that the shield is reusable and does not retain its own magnetization.

Chapter 3: Prior Art

Section 3.1: Materials and Methods

Several methods have been demonstrated in literature to achieve the necessary magnetic shielding for a variety of unique applications ranging from high precision spin precession measurements to noise reduction in magnetic random-access memory. Due to the wide range of applications, various materials and manufacturing methods have been used based on the unique demands for each project. Table 3.1 lists the relevant parameters of the materials commonly used in magnetic shielding applications ordered by the maximum relative permeability [20][24][25][26] [27][28][29].

It should be noted that these reported values of relative permeability are only achievable under specific conditions for maximization. Specifically, amorphous metals must be magnetically annealed, a process by which they are heated in a furnace and cooled. Annealing under specific conditions rearranges atoms locally, changing the stress profile to favor magnetization in the direction that the material is intended to be used [23]. Several studies have investigated the optimal conditions under which to perform the anneal, such as in inert atmospheres or with specific ramp up and down temperatures [26]. Furthermore, other methods have been shown in literature for actively maximizing the permeability of these shielding materials in operation, such as field shaking [20]. By applying a large, alternating magnetic field on top of the external field to be shielded, the domain walls in the material are constantly in motion and less likely to become frozen by the interference of a lattice defect. It has shown to improve permeability by over a factor of two, which becomes a significant effect on the multiplicative shielding factor of multilayer shields.

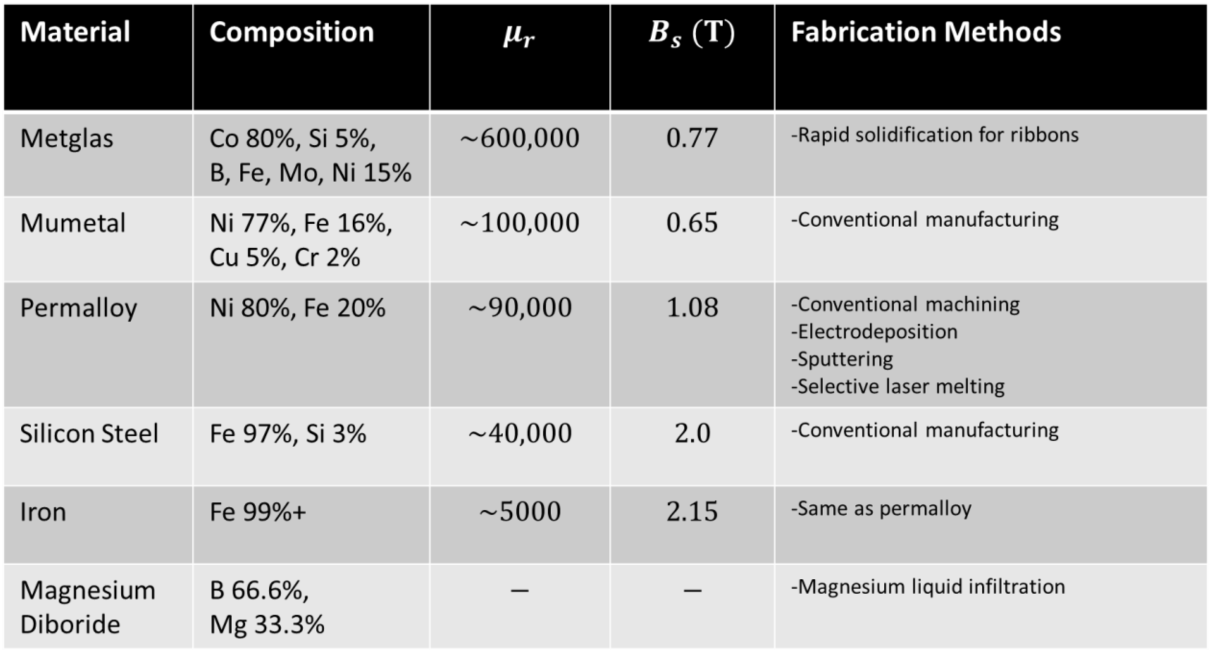

Material	Composition	μ_r	B_s (T)	Fabrication Methods
Metglas	Co 80%, Si 5%, B, Fe, Mo, Ni 15%	~600,000	0.77	-Rapid solidification for ribbons
Mumetal	Ni 77%, Fe 16%, Cu 5%, Cr 2%	~100,000	0.65	-Conventional manufacturing
Permalloy	Ni 80%, Fe 20%	~90,000	1.08	-Conventional machining -Electrodeposition -Sputtering -Selective laser melting
Silicon Steel	Fe 97%, Si 3%	~40,000	2.0	-Conventional manufacturing
Iron	Fe 99%+	~5000	2.15	-Same as permalloy
Magnesium Diboride	B 66.6%, Mg 33.3%	–	–	-Magnesium liquid infiltration

Table 3.1: Table comparing the composition, maximum relative permeability, saturation magnetization, and available fabrication methods for various materials used in magnetic shielding [20][24][25][26][27][28][29].

Metglas is a promising material that has been used for low frequency magnetic applications in the past few decades. It has a proprietary composition consisting primarily of cobalt, which enables the highest reported relative permeability of any material in literature at around 600,000, making it very attractive for shielding. The manufacturing method for Metglas involves rapid solidification. The heated amorphous metal is spun out rapidly and cast into a ribbon form, which makes it easy to wrap around existing shapes for shielding. However, this is currently the only available form of Metglas, meaning it can be difficult to apply for certain geometries or situations where a hard mold is necessary. Furthermore, as it is a proprietary material, it is a more expensive option. Thus, its use in magnetic shielding literature has been less widespread.

On the other hand, mumetal has been the most common material for magnetic shields at nearly all size scales. It should be noted that while it is primarily a nickel and iron alloy, several different vendors sell their own proprietary composition, which contains varying amounts of copper, chromium, molybdenum, and silicon. Each stoichiometry offers slight variations in its magnetic properties, but an upper estimate of 100,000 relative permeability is found in literature. While its permeability is lower than that of Metglas, its lower cost and ease of manufacturing have made it the most pervasive material for constructing magnetic shielding. It is compatible with all methods of conventional machining, such as rolling, stamping, molding, etc., allowing it to be formed into the desired shape for shielding. However, the extremely high permeability paired with the lower saturation magnetization means the geometry must be catered to the specific application. A thicker layer of iron or ferrite is often placed around mumetal shields to lower the external flux density that the mumetal directly contacts.

Without the various additional elements added to form mumetal, the nickel-iron alloy base is known as permalloy. While the specific composition ratio can vary depending on the vendor or application, it is primarily found in the 80-20 ratio. Certain additives tend to increase the relative permeability of permalloy, but the greater iron content offers a higher saturation magnetization. Most importantly, permalloy is a much simpler alloy, meaning it is not only cheaper but can also be purchased or manufactured using several different methods beyond conventional machining. A common method of depositing thin layers of permalloy is direct current (DC) magnetron sputtering. Ionized gas molecules bombard a target material, releasing vaporized metal atoms into a plasma which physically coat a surface. The process is inexpensive and can be done in batch, but the sputtering rate is extremely slow on the order of nm/min [30]. Thus, it has mostly been explored for thin, multilayer EMI shields that can take advantage of multilayer reflection. A recent demonstration used selective laser melting, a form of additive manufacturing, to print permalloy shields to be used in spacecraft gyroscopes [27]. This method allows customized geometries to fit specific component shapes that normally could not be achieved with conventional machining. However, this method is unable to take advantage of multilayer shielding factors as two metals cannot be simultaneously and precisely deposited. On the other hand, the stoichiometry of permalloy lends itself to electrodeposition, a process by which metal can be uniformly deposited onto a conductive surface in a salt bath via an electric current. This promising method for multilayer shielding has been used extensively in micro-scale magnetic systems and will be elaborated on in Chapter 5 [31].

The remaining materials in the table are less prevalent and mostly used for very specific applications. Silicon steel and iron have large saturation magnetizations and are used in applications for shielding extremely large fields, such as those generated by magnetic resonance imaging (MRI) [32]. The cheaper material cost is useful in constructing large rooms containing equipment generating strong magnetic fields. Finally, magnesium diboride is a unique, inorganic compound that has only recently been studied for magnetic shielding. At 4.2 K, the material behaves as a superconductor and is able to shield extremely low frequency magnetic fields using eddy currents [29]. As these materials essentially shield with image charges, they do not saturate and can function for very high external flux densities. While useful in certain applications such as SQUID, they are not viable for most shielding applications that do not operate under cryogenic conditions.

Section 3.2: Shielding Factors

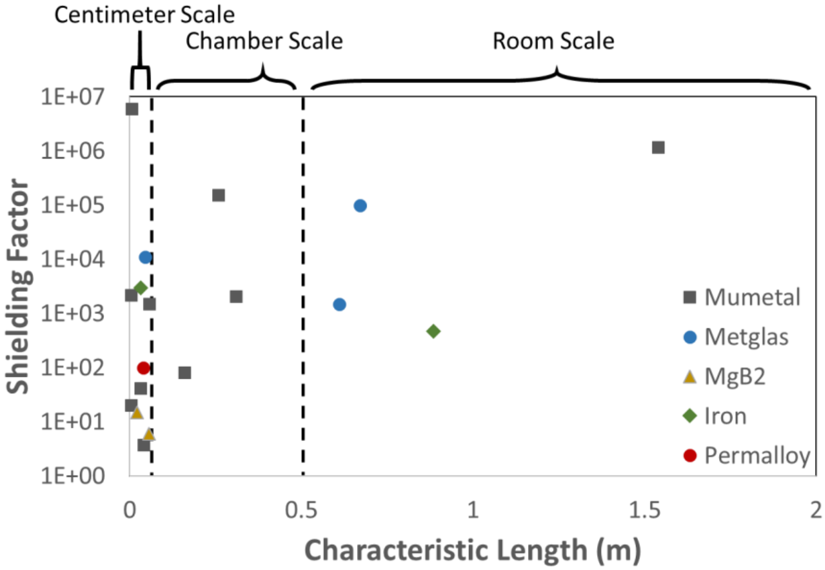

Figure 3.1: White space chart of shielding factors reported in literature compared to the characteristic lengths of shielding [19][29][33][34][35][36][37][38][39][40][41][42][43][44][45].

Figure 3.1 shows the shielding factors of several fabricated magnetic shields reported in literature to the characteristic lengths, which is the longest dimension in the direction of shielding [19][29][33][34][35][36][37][38][39][40][41][42][43][44][45]. In the case of a cylinder, for example, the characteristic length is plotted as the diameter of the innermost shield. As mentioned before, the magnetic shield size and shielding factor must be catered to the specific requirements of each project. Thus, the chart is divided into three sections based on the intended use of the shield.

Firstly, for shields above half a meter in characteristic length, the purpose is often to create a nearly room-scale magnetic shield. Altarev et al. created a magnetically shielded room for the purposes of investigating neutron EDM, which requires temporal stability of magnetic gradients better than 3 pT/m over 300 s [34]. The room was constructed from five shielding layers of 3 mm-thick mumetal with the largest shield being nearly 3 m in each dimension. A transverse shielding factor of around 1,200,000 was reported. A diagram of this shield is shown in Figure 3.2. However, such expensive amounts of mumetal are not always necessary for room-scale shields. Saito et al. reported a shield consisting of aligned strips of silicon steel to inexpensively shield an MRI room [41]. While the shielding factor was lower at only 475, the investigation demonstrated a practical solution for simultaneously containing the field from an MRI while also providing relief for claustrophobic patients.

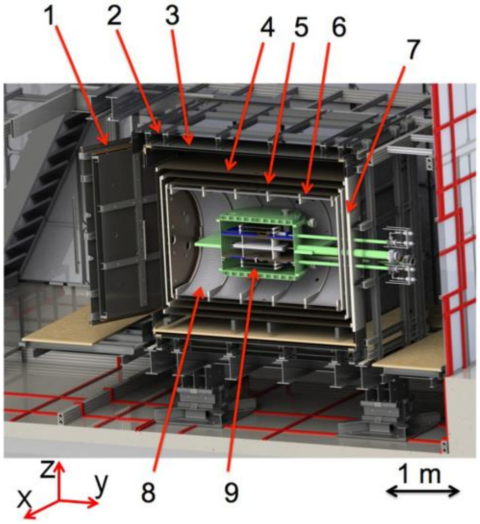

Figure 3.2: Room-scale magnetic shield fabricated for neutron-electric dipole moment measurements [34].

Several publications are interested in understanding or optimizing shielding factor at the chamber scale for experimental measurements. Freake et al. were interested in designing a shield to fit in a dilution refrigerator to screen Earth's magnetic field to below 5 nT. By constructing a three 1.6 mm-thick layer mumetal shield, the largest with a 29 cm diameter, a shielding factor of 150,000 was obtained for their application [43]. More recently, Malkowski et al. studied methods for reducing the flux leakage across the gap between a cylindrical shield and its endcap [40]. By adding a thin foil of magnetic material that overlaps the two surfaces, a single 1.6 mm-thick mumetal prototype with a 31 cm diameter achieved an impressive shielding factor of 2,064. Figure 3.3 shows a photo of this cylindrical shield.

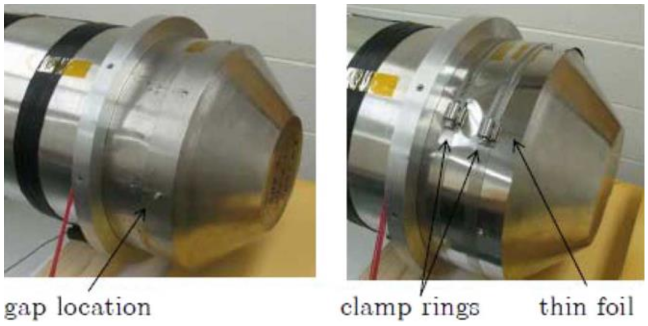

Figure 3.3: Chamber-scale magnetic shield with clamp rings holding a thin foil in place between the cylinder and its endcaps to reduce flux leakage [40].

Recent interest in magnetometers such as SQUID has led to studies of superconducting magnesium diboride shields. Gozzelino et al. investigated the longitudinal shielding capability of two layered 1 cm cups of magnesium diboride and iron to achieve a shielding factor of 15 [45]. Arpaia et al. performed a similar study with a single 5.6 cm cup of magnesium diboride for a shielding factor of 6 [29]. While the shielding factors themselves are low, it should be noted that the externally applied fields are on the order of 1 T, which would typically immediately saturate Metglas or mumetal shields.

Section 3.2.1: Millimeter-Scale Shielding Factors

While magnetic shielding is relatively well explored in the macroscale for high fidelity, low noise rooms or measurement chambers, miniaturized solutions have yet to meet the various demands of chip-scale shielding. Though theory might suggest that decreasing characteristic length would yield higher shielding factors, the trend in Figure 3.3 shows that obtaining high shielding factors for sub centimeter-scale shielding can be relatively challenging with some exceptions. Ultimately, the reason is two-fold: portable shields generally do not have large shielding factor requirements and conventional shielding fabrication methods are challenging for small sizes.

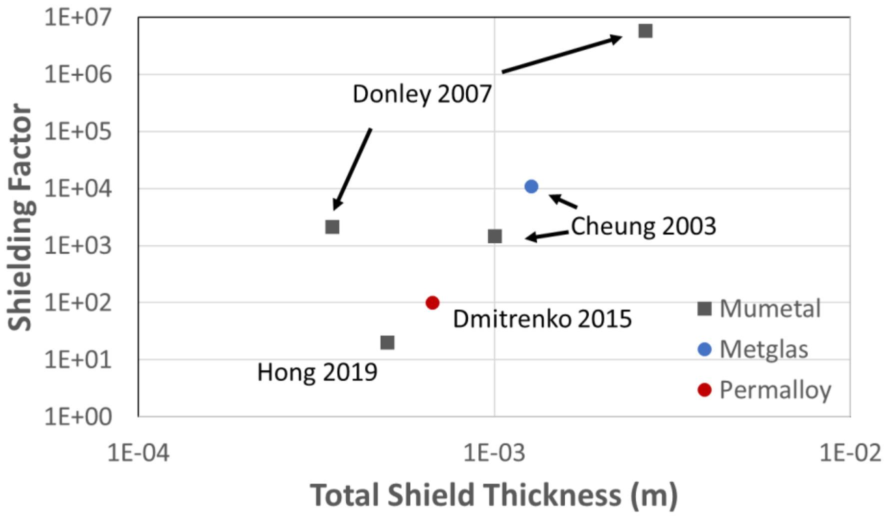

Figure 3.4: White space chart of centimeter-scale characteristic length shields plotted with shielding factor reported in literature to total shield thickness [19][35][37][38].

Figure 3.4 shows literature in the sub-cm characteristic length regime and plots the shielding factor to total shield thickness, which is the shield thickness from the inner diameter of the innermost shield to the outer diameter of the outermost shield [19][35][37][38]. Cheung et al. reported the largest of these shields in terms of characteristic length in the 4 to 6 cm range [35]. This study aimed to compare the effectiveness of Metglas compared to mumetal shielding for a small-scale neutron EDM measurement. Overall, Metglas proved more effective by providing 11,000 transverse shielding factor compared to 1,471 for a single mumetal shield. However, the Metglas layer was unoptimized, consisting of 50 layers wrapped around a cylinder, which allowed flux to leak through the slits between ribbons. The simplest shield is reported by Hong et al. for isolating a chip-scale atomic clock from nearby biasing circuitry [37]. The shield was formed by primitively stacking mumetal pieces to form a hollow cube and provided a shielding factor of 20. While enough to reduce frequency instability from a small 30 µT field, larger external noise sources would require significant further optimization.

Perhaps the most efficient shielding was demonstrated by Donley et al. by stacking five layers of cylindrical mumetal shields [19]. The shields are shown in Figure 3.5. The smallest cylinder had a 4.1 mm diameter with a 350 µm thickness, providing a transverse shielding factor of 2,154. While the reduced field within all five shields stacked together could not be measured, three shields provided an enormous 5,900,000 shielding factor. However, the outermost shield had a volume of 3 cm^3, preventing this layering technique from being integrated at the chip-level. Furthermore, individual wires must be threaded by hand with conventionally manufactured shields making interconnect extraction through pinholes challenging.

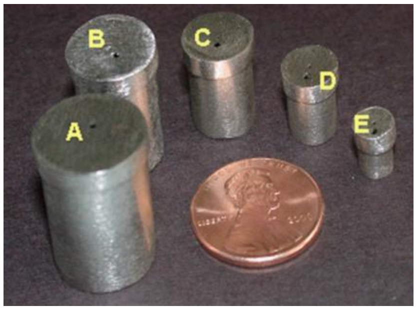

Figure 3.5: Centimeter-scale multilayer mumetal shields fabricated using conventional machining methods compared to the size of a penny [19].

Electrodeposited magnetic shields have also been explored by Dmitrenko et al. for shielding photomultiplier tubes (PMTs) to prevent the trajectory of photoelectrons from being altered by undesired magnetic fields [38]. Alternating layers of permalloy and copper were deposited on conductive aluminum PMT mounts with 37 mm diameters and resulted in shielding factors of around 100 with 500 µm of total shielding thickness. Figure 3.6 shows the plated PMT mounts. This method of electrodeposited shielding was applied to a large mount and not optimized for batch fabrication.

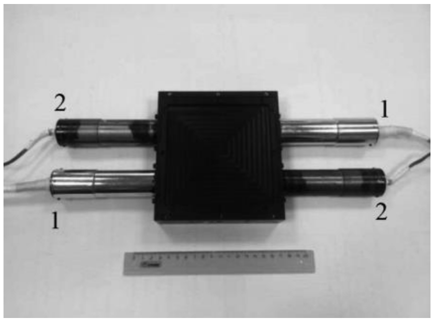

Figure 3.6: Electroplated multilayer permalloy and copper shields on a 37 mm diameter photomultiplier tube mount compared to a 20 cm-long ruler [38].

Section 3.3: Advantages of Batch Electrodeposited Shielding Layers

Magnetic shields become very challenging to implement when scaling down to centimeter or millimeter characteristic lengths. The largest hurdle is the limitation of conventional machining methods at smaller size-scales. In order to fabricate a mumetal shield, the sheets of metal must be individual machined into a custom shape while leaving enough space for endcaps. Furthermore, to take advantage of multilayer shielding, these shapes must be stackable by hand while interconnects must be extracted manually through small pinholes to maximize shielding efficiency. While these methods are acceptable at larger scales for one-off type applications in room construction or equipment, this becomes infeasible for batch manufacturing or packaging for a large number of devices.

On the other end of the spectrum, DC magnetron sputtering is a mature technology used even in industry for conformal metal deposition. Sputtering equipment is also able to load multiple targets at once, allowing multilayer films of permalloy and non-magnetic materials such as copper to be conveniently stacked. However, the deposition rates are extremely slow, taking several hours to sputter only microns of film. As the film thicknesses provide insufficient shielding for low frequency fields, studies have largely been limited to micron-thick multilayers at MHz and above frequencies, where the shielding mechanism switches from flux redirection to eddy currents and electromagnetic wave scattering [28][30].

Thus, electrodeposition is the most compelling choice for the purpose of maintaining high shielding factors at small scales. Glickman et al. has previously demonstrated electroplating of high permeability ($\mu_r > 8000$), high saturation ($B_s > 1$ T) permalloy for batch fabrication of microelectromechanical systems (MEMS) [31]. These deposition rates can be up to two orders of magnitude faster than those of sputtering, allowing relevant thicknesses for the purposes of low frequency shielding. To achieve multilayer shielding, commercial copper baths are readily available to plate copper as the spacer layer between magnetic shields for rapid laminations. The materials are uniformly deposited onto the target, circumventing any issues with manual assembly and simultaneously allowing sophisticated interconnect extraction schemes, such as winding or snaking paths. The potential contamination of copper in permalloy as a result of rapidly alternating plating has also been shown in literature to improve magnetic properties by reducing the crystal anisotropy and magnetostriction of permalloy [46]. Furthermore, electrodeposition can be easily integrated into silicon microfabrication processes to optimize for even smaller shield sizes and to reduce costs through parallelism. Ultimately, permalloy electrodeposition can address the various hurdles faced by miniaturizing magnetic shielding, providing a realistic solution to achieving true “AMO on a chip” systems.

Chapter 4: Design

Section 4.1: Finite Element Method Simulations

A magnetic shield is designed to either protect a system from external fields or to contain the fields within a system from significantly leaking to the outside environment. Thus, the requirements for shielding in an AMO chip application are two-fold: size and shielding factor. First, it is necessary to define the area or volume that needs to be contained within the shield. It is also critical to consider the size of the total shield thickness that can be used in a given application. Then, given that particular geometry, which relates to the characteristic length of shielding, the shielding material and thickness must be capable of providing adequate shielding factor.

Design of an electroplated magnetic shield begins by analytically estimating the shielding factor that can be attained for a particular shield size and total shield thickness. However, as indicated in Chapter 2, magnetic shielding theory often makes several approximations as it is challenging to find closed form solutions of realistic shield geometries. As such, it is more practical to utilize numerical methods to calculate the shielding effectiveness of various designs. In this work, COMSOL Multiphysics was selected as the software of choice due to availability and familiarity of the author. COMSOL is a 3-dimensional (3D) multiphysics simulation software that uses the finite element method (FEM) to analyze several coupled systems of partial differential equations. Specific to magnetic shielding, it is capable of numerically solving for magnetic fields in the presence of arbitrary shapes of magnetic material. A powerful tool that can be incorporated in COMSOL simulations is the definition of nonlinear magnetization curves for different materials. While simulations can be run with constant permeability values, COMSOL can numerically solve for the relative permeability of a magnetic material depending on the external field, which is critical in modeling the magnetic saturation. This is especially important in multilayer shields where each shielding layer experiences a different level of magnetization as outer layers are much more likely to reach magnetic saturation than inner layers.

Figure 4.1 shows a 3D COMSOL simulation of a cylindrical shield of electrodeposited permalloy in the presence of a 15 mT background magnetic field, the higher end of background field expected in an AMO system. The shield is designed with a 6.5 mm inner diameter and 300 µm total shield thickness. This simple, single layer shield is able to achieve a transverse shielding factor of 215. From Chapter 2, shielding factor of this cylinder can be estimated as 325, which yields a relative error of 33.9% between the simulated and analytical solutions. Given the finite height of the cylinder, which reduces the shielding factor from the idealized equation, it can be concluded that the COMSOL simulation result is sufficient for estimating the shielding factor of more complex shape geometries. Thus, it is the primary tool that will be used in evaluating the effectiveness of shields designed for the various applications in this work.

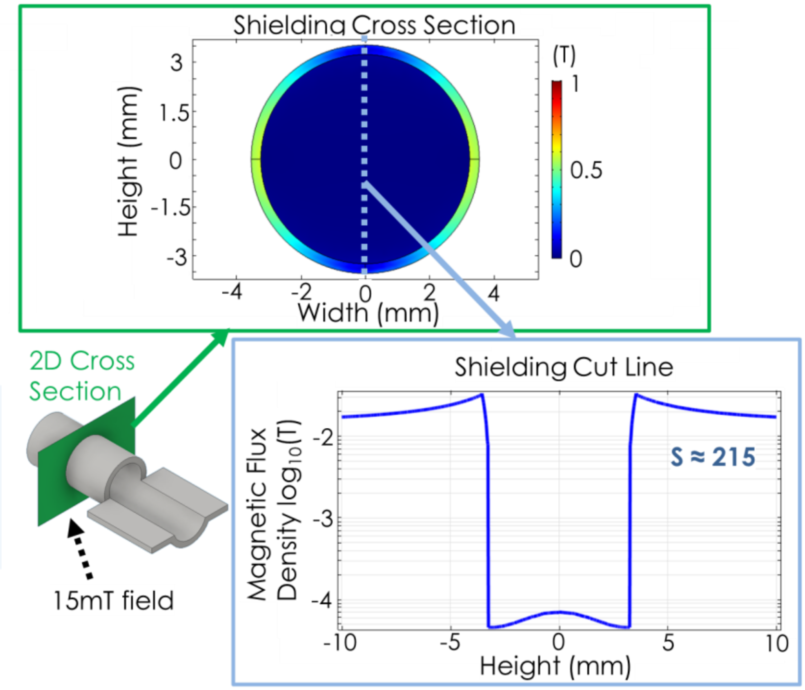

Figure 4.1: COMSOL simulation of a 15 mT field applied to a shield with 6.5 mm inner diameter and 12 mm length. The cross section (green) shows the material is not yet saturating, and the cut line (blue) shows a shielding factor of 215.

While a full 3D simulation is most likely to accurately characterize a real, physical system, it can be difficult to have them converge in practical runtimes. Several factors can affect the simulation time and trading them off can result in the solver failing to reduce the error and converge to an accurate solution. In the context of this work, 3D simulations can be altered to 2D or 2D axial simulations to reduce the simulation load. Furthermore, the ratio between the characteristic length and minimum shield layer thickness is important to consider as the latter reduces the maximize mesh size allowed. A large ratio thus results in a simulation with an extremely dense mesh over which the solution must converge. This effect is worsened in multilayer shield simulations, where the permeability rapidly alters over different nodes in the mesh. Finally, though preferred to simulate more realistic shielding behavior, the usage of nonlinear magnetization curves also worsens simulation runtime and convergence. The various simulations used in this work attempt to optimize for these factors, meaning full 3D simulations with nonlinear hysteresis for some geometries simply cannot be utilized.

Section 4.2: Sub-Millimeter Shielding Factor

As electroplated permalloy aligns itself and deposits via electric currents, the shield can be shaped around volumes much smaller than feasible with conventional machining methods. As the shielding factor scales inversely with characteristic length, it is theoretically possible to attain previously unrealizable shielding factors. Electrodeposition can be easily integrated within surface or bulk micromachining steps, taking advantage of existing tools to create these small volumes. These methods will be elaborated on further in Chapter 5. Thus, the shield sizes and thicknesses in this section are designed around those of typical silicon wafers.

Figure 4.2 demonstrates a simulation of a flat, cylindrical five-layer permalloy shield. The inner diameter is 2 mm and the longitudinal height is 500 µm. The layer thicknesses are 50 µm with 50 µm spaces between each layer. The field applied in the simulation is 15 mT. The permeability in this model is dynamically calculated from a magnetization curve measured by

Glickman et al. [31]. It can be seen that the corresponding longitudinal and transverse shielding factors far exceed those reported experimentally in literature at 170,000,000 and 100,000,000, respectively. While it is typically expected to have a greater transverse than longitudinal shielding factor, the flat nature of the cylinder results in a shorter effective characteristic length in the longitudinal direction. Also, due to 3D simulation challenges, each cut-plane is actually a separate 2D axisymmetric simulation, meaning the transverse direction shielding factor is actually approximated with that of a sphere, further explaining the discrepancy.

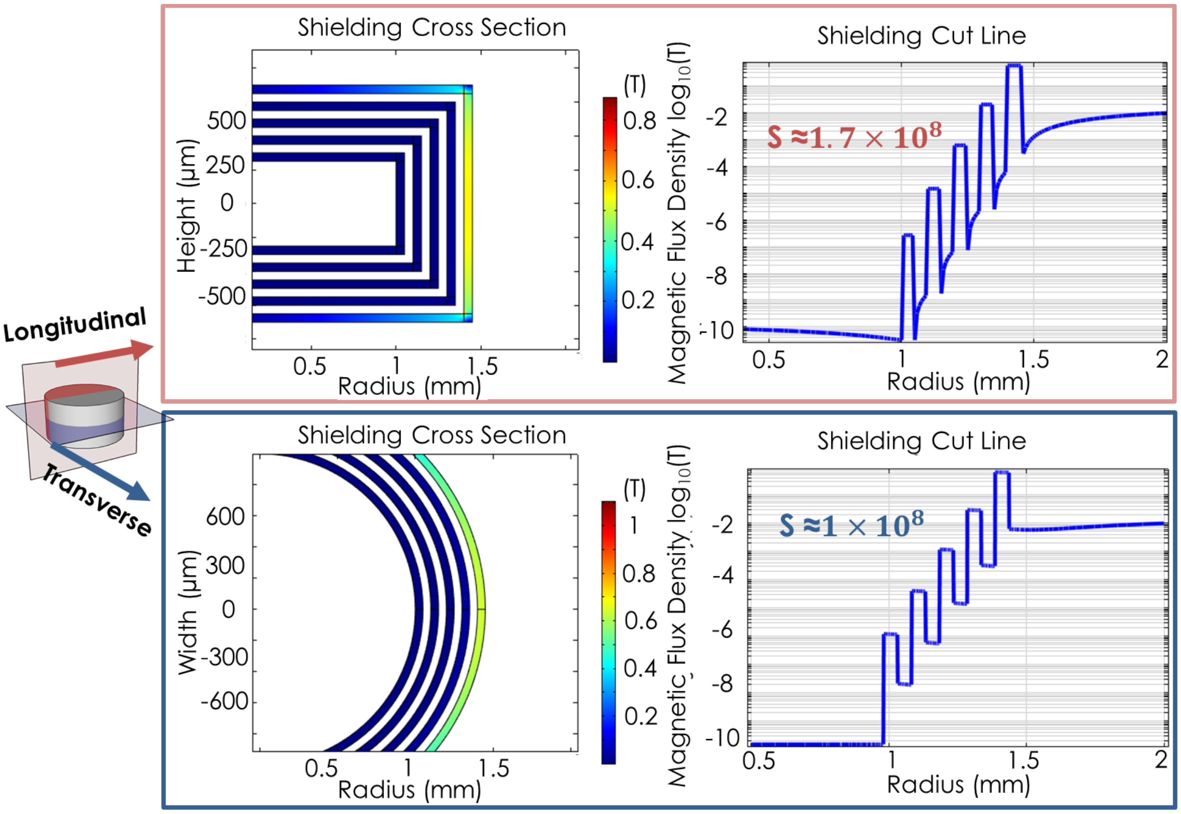

Figure 4.2: COMSOL simulation with nonlinear magnetization curves for a 2 mm inner diameter and 500 µm tall multilayer magnetic shield. The total shield thickness is 450 µm with five 50 µm layers separated by 50 µm each. Longitudinal (red) cross section shows a 170,000,000 shielding factor. Transverse (blue) is simulated with a sphere instead of a true transverse cross section due to axisymmetric limitations, but achieves a 100,000,000 shielding factor.

It should be noted that the shielding factors predicted by simulations represent theoretical maxima, but various experimental factors often mean the resulting measurements may not yield such ideal values. For example, while numerical estimates can be used to design for these unprecedented shielding factors, measurement of these shielding factors yields a challenge of its own. The shields have an internal flux density of 0.15 nT, a resolution difficult to achieve with even calibrated atomic magnetometers. Furthermore, the magnetometer would need to fit within the miniaturized sub-millimeter shield, resulting in a shielding factor that would be experimentally unfeasible to verify with the resources available.

Section 4.3: Simulated Multilayer Shielding Trends

As mentioned in Chapter 2, multilayer shields can provide high scaling shielding factors only when the layer thicknesses and characteristic lengths are appropriate. Thus, parametrized COMSOL simulations were used to design various millimeter and sub-millimeter-scale shields, investigating the regimes where multilayer shielding was effective.

Section 4.3.1: Millimeter-Scale Shielding Trends

Millimeter-scale shields are similar in characteristic length and height to the most compact shields that have been demonstrated in literature so far. Thus, it is appropriate to verify the trends achievable with electrodeposited permalloy. Figure 4.3 shows longitudinal shielding factor simulations of 1 cm tall cylinders with 300 µm and 500 µm total shielding thickness plotted against a changing inner radius. The spacing between multilayer shields is the same as the thickness of individual shields. It is evident that the shielding factor decreases as radius increases in all cases, which is to be expected with the trends outlined in Chapter 2.

However, the simulations also reveal a dependence of shielding efficiency with the radius as well. At 1 mm, multilayer shields outperform single layer shields by 17% for 300 µm shields and 61% for 500 µm shields. As the total shielding thickness increases, the effect of multilayer shields on shielding factor is expected to increase as the total product of shielding scales much faster. As the radius increases, the thinner layers no longer act as strong individual shields resulting in a lower combined product. Eventually, at a 2 mm radius, the single layer shields provide nearly the same shielding factor as multilayer options. Thus, it is important to factor in the size scale of the shielded volume as well as the individual shielding layers when considering the design of multilayer shields.

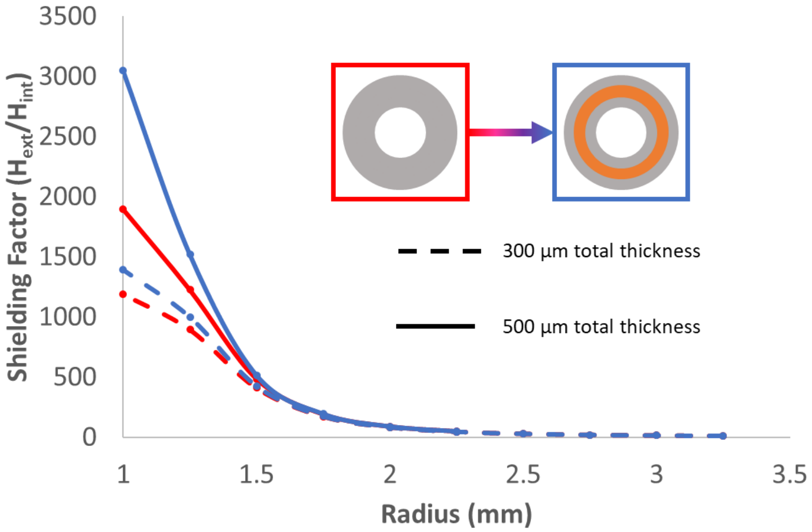

Figure 4.3: Plot of simulated longitudinal shielding factor to inner shield radius for cylindrical shields with 12 mm height and 300 µm (dashed) or 500 µm (solid) total shielding thickness with one layer (red) or two layers (blue).

Section 4.3.2: Sub-Millimeter-Scale Shielding Trends

Simulations were also run to investigate the trends of multilayer shielding at the sub-millimeter-scale. Figure 4.4 shows the results of a suite of simulations using a 1 mm tall shield with 50 µm total shielding thickness. The longitudinal shielding factor trend was plotted against increasing shield radius from 500 µm to 3 mm for shields with 1, 2, and 3 shielding layers, each separated by the same spacing as the respective shield thicknesses. The longitudinal shielding factor is investigated here as the flatter geometry of the shielded volume is intended for axial shielding.

Similar trends reveal themselves at the sub-millimeter size scales as well. At 500 µm, multilayer shields are superior to single layer shields by several orders of magnitude with three-layer shielding achieving a 10,600 longitudinal shielding factor compared to 252 from a single layer. At a 2.5 mm radius, due to the lowered individual shielding factors, the single layer shields again perform equivalently to the multilayer shields. Regardless of the shielding direction or size scale, shields must be designed to properly take advantage of multilayer multiplicative shielding factors. This is yet another advantage of electroplated shields as the shield thickness and shape design can be easily tuned during fabrication.

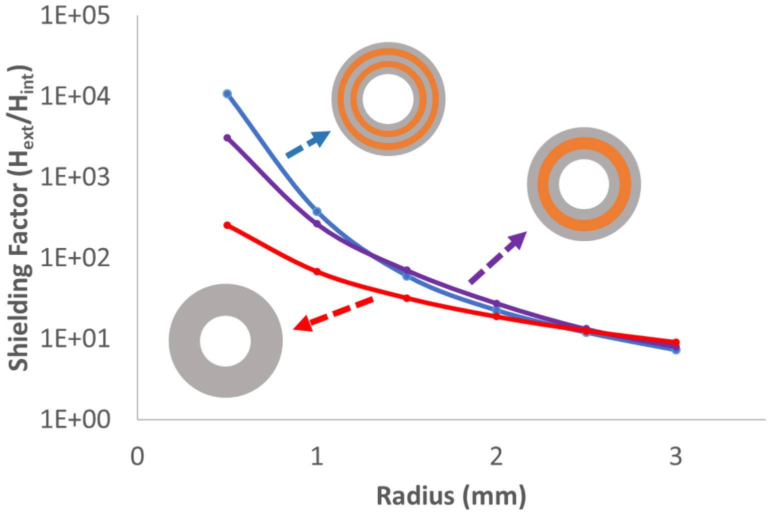

Figure 4.4: Plot of simulated longitudinal shielding factor to inner shield radius for flat cylindrical shields with 1 mm height and 50 µm of total shielding thickness for one layer (red), two layer (purple), and three layer (blue) shields.

Section 4.3.3: Incomplete Shields

In order to fabricate the flat, sub-millimeter shield, permalloy and interstitial copper layers must be sequentially electrodeposited on both sides of the device simultaneously. Due to the nature of packaging, this is not necessarily a feasible solution. Thus, simulations were run to investigate an alternative package where the bottom layers of a shield are deposited prior to the top layers. This results in shielding layers which do not form complete flux loops and can negatively impact the shielding factor.

Figure 4.5 shows the results of shielding factor simulations of various total shield thicknesses around a cylinder with 1 mm inner diameter, 100 µm height, and 10 µm permalloy shielding layers separated by 10 µm each. The green line shows the shielding factor growing exponentially as expected with total shield thickness as the shield layers are not yet saturating. However, the red line shows the shielding factor trend with an incomplete shield which begins to saturate. Since the flux lines are mostly shunted through the first shielding layer on the top half, the shielding factor growth does not continue on the expected trend. However, it is possible to mitigate this effect with the introduction of thicker layers of the shield where flux is expected to saturate. This effect is shown in the blue line by thickening both the inner and outermost layers of the top and bottom half shields to 30 µm. While this does increase the total shield thickness, it is possible to delay the shielding factor saturation by an order of magnitude.

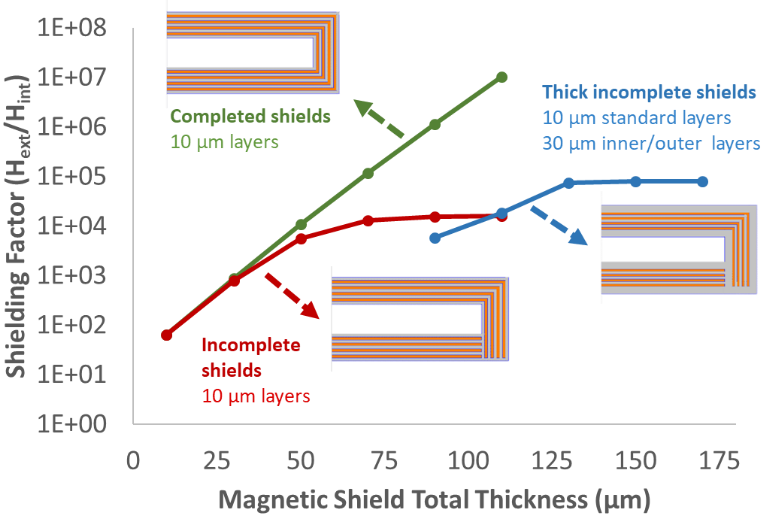

Figure 4.5: Simulated longitudinal shielding factor to total magnetic shield thickness for cylindrical shields with 1 mm diameter, 100 µm height, and 10 µm shields separated by 10 µm each. Completed shields (green) indicate better scaling with total thickness than incomplete shields (red), but thickening both the innermost and outermost shield layers to 30 µm (blue) recovers an order of magnitude in scaling.

Section 4.5: Inverted Shielding Factor

Section 4.5.1: Contained Coil Shielding Factor

Due to the challenge of characterizing such a shield with an external magnetic field, the inverse situation was considered in which the millimeter-scale shield is used to contain a magnetic field source. Thus, simulation results were studied where sets of planar coils were inserted within the shield, and the external flux density was measured. Figure 4.6 shows a COMSOL simulation with four pairs of 100 mA coils placed within a flat, cylindrical three-layer permalloy shield. To better mimic the parameters achievable in a realistic microfabrication process, the shield has an inner diameter of 2 mm and 100 µm height with three 10 µm shielding layers separated each with 10 µm for a total of 50 µm of shielding thickness.

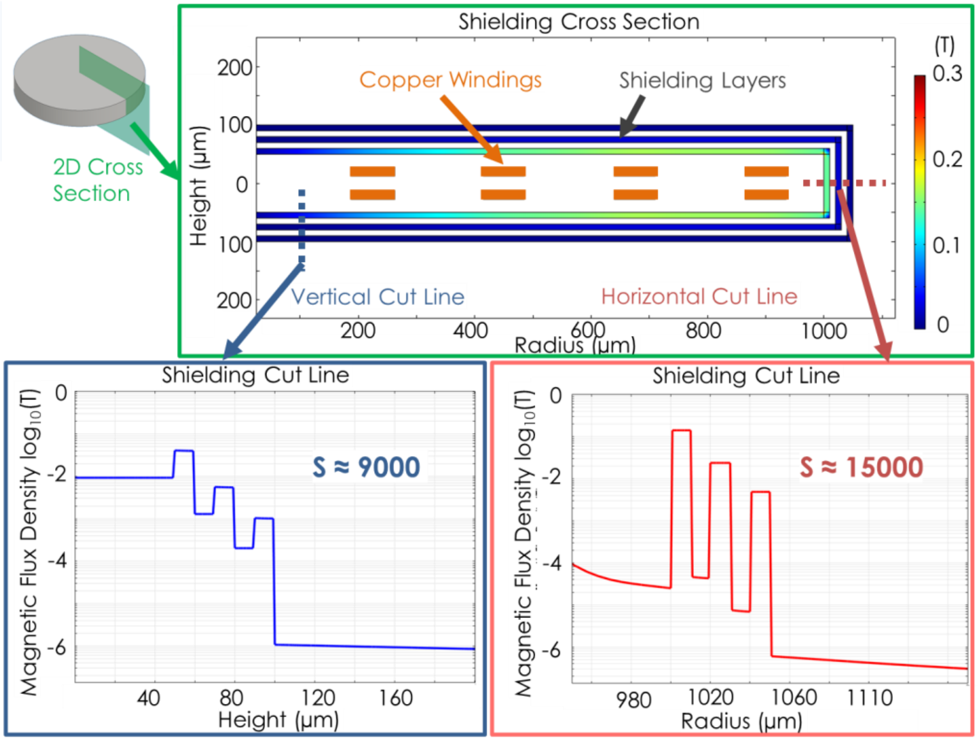

Figure 4.6: COMSOL simulation of a 1 mm diameter, 100 µm height multilayer shield with three 10 µm layers separated by 10 µm each. Field is applied using 16 coils distributed within the shield (green). The longitudinal cutline (blue) shows a 9,000 shielding factor while the transverse cutline (red) shows a 15,000 shielding factor.

The achievable shielding factor is relatively high with the longitudinal shielding factor reaching 9,000. It should be noted that the shielding factor is calculated by the ratio between the internal and external field and can vary depending on the coordinate from which the internal field generated from the coil and the field external to the shield is analyzed. This is because the field at all points is expected to change with the introduction of a soft magnetic material. In this calculation, the field is taken at the inner edge of the shield at 100 μm from the center to avoid artifacts at the very center. The external field is taken immediately at the outer edge of the shield and continues to drop off further away. On the other hand, the "transverse" shielding factor is calculated as 15,000 and is derived from the same internal field but with the external field at the outer edge of the shield in the transverse direction. This is better described as the longitudinal shielding factor in the radial direction since the internal field is still in the longitudinal direction. This likely overestimates the shielding factor as the internal field would have dropped off significantly simply with distance away from the center.

Section 4.5.2: Contained Permanent Magnet Shielding Factor

While shield design with a contained magnetic coil may be useful for characterization, the more realistic situation for an AMO system is for a shield to contain permanent magnets. One example is a Penning trap, which stores charged particles by superimposing an inhomogeneous quadrupole electric field on a homogeneous axial magnetic field. A large electric field can be applied to these trapped ions to sputter titanium getters that react with atmospheric gas molecules. With an array of Penning cells, researchers have demonstrated miniaturized, chip-scale vacuum pumps necessary to realize a miniature atomic clock [47]. Thus, in packaging these pumps near other AMO systems, it is critical to prevent the homogeneous magnetic field from leaking out.

Figure 4.7 investigates the effectiveness of electroplated permalloy shields to contain the fields from permanent magnets. The 2D axisymmetric simulation encases two 250 mT cylindrical neodymium magnets in five permalloy shielding layers. The permanent magnets have 1.6 mm diameter and 800 μm height. The shields have a 1.7 mm diameter with 25 μm thick layers and spacing. The longitudinal shielding factor is calculated to be 40,000 with the internal field determined by the field of the permanent magnet. Similarly, the radial shielding factor is calculated to be 45,000. The simulation results show that corners of the initial shielding layers will be saturated from the intense magnetic flux density of the permanent magnets, but outer layers can continue to sustain the remaining flux, thereby maintaining a large shielding factor. Realistic geometries of the shielded Penning trap would include fluidic interconnects and cutout holes for the sputtering anode, lowering the effective shielding factor. However, such pinholes will not isolate the shields entirely and will only affect flux redirection locally. Overall, permalloy multilayers electroplated directly onto chip-scale AMO systems can offer ease of alignment while still maintaining substantial shielding factors for isolating relevant permanent magnets.

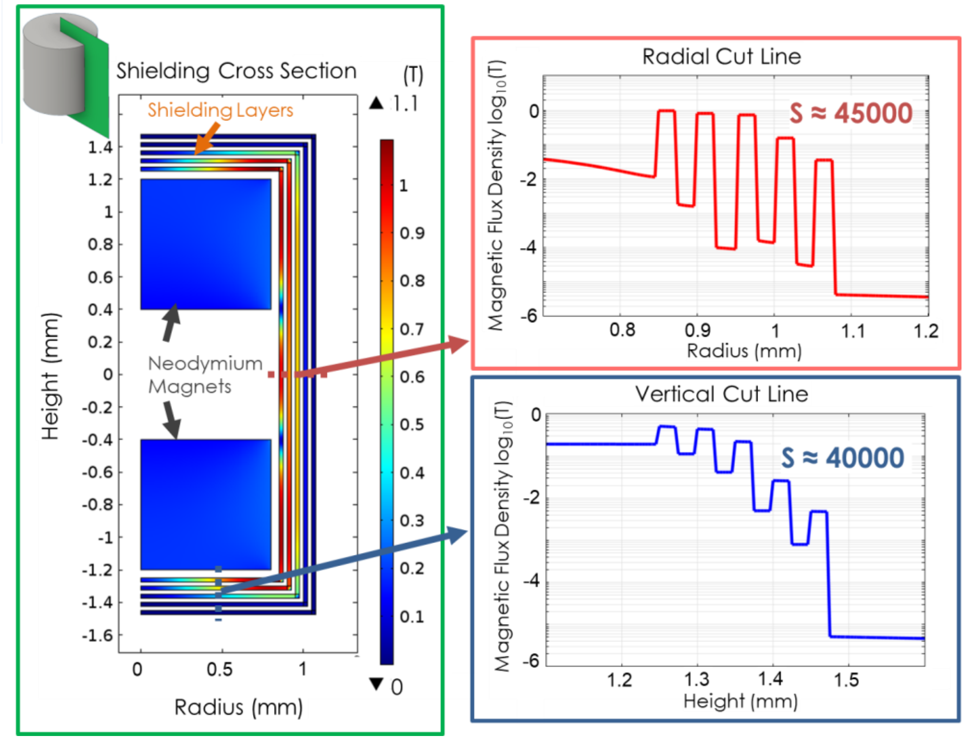

Figure 4.7: COMSOL simulation of two 250 mT cylindrical permanent magnets for a Penning trap encased by a five-layer shield with 25 μm-thick layers (green). The longitudinal cutline (blue) shows a 40,000 shielding factor while the transverse cutline (red) shows a 45,000 shielding factor.

Section 4.5.3: Effect on Contained Permanent Magnets

Beyond permanent magnets used in ion traps, AMO systems also use optical isolators to prevent lasers used to interrogate atomic transition energies from scattering backwards and potentially affecting the laser quality or other systems. Once again, magnetic fields are necessary to realize these devices. For this application, the permanent magnet must have a bore through its axial center to allow light to pass through. Figure 4.8 shows the simulation of a single layer shield on the field profile of a 10 mT optical isolator magnet with 8 mm diameter and 1.4 mm bore diameter. The shield has a 9 mm inner diameter and consists of a 700 µm permalloy layer with no caps to avoid interrupting the on-axis field. The shield serves to contain the flux density of the magnet without approaching saturation due to the thickness of the permalloy layer.

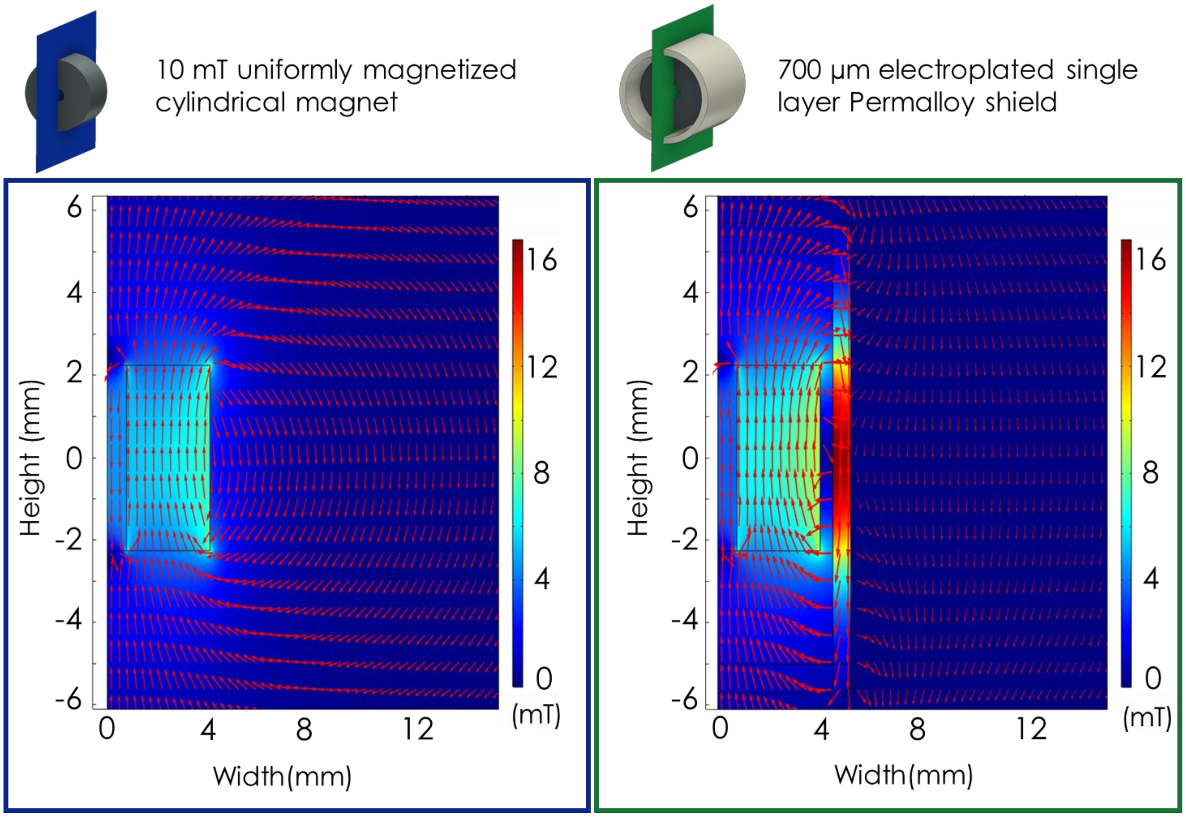

Figure 4.8: COMSOL simulation of a 10 mT optical isolator magnet with a 1.4 mm bore (blue). A separate simulation with a 700 µm permalloy shield with 9 mm diameter demonstrates field homogenization outside the shield (green).

Figure 4.9 compares the radial cutline of the magnet contained by a 700 µm permalloy shield as well as a two-layer permalloy shield with 300 µm layers and 100 µm separation totaling to 700 µm of total shielding thickness. The target was to reduce the flux density of the magnet by one order of magnitude within a centimeter, so the shielding factor was calculated by taking the ratio of the unshielded to shielded fields at all points. The maximum shielding factor can still be calculated by taking the ratio at the immediate outer surface of the shield. However, this characterization of shielding factor causes the effective shielding to drop off radially as the permanent magnet field inherently decreases. Both designs are capable of sustaining the target shielding factor of 10 beyond 15 mm from the center of the magnet. The multilayer shield is capable of providing higher shielding factor at close distances to enable more compact integration of magnetically sensitive components.

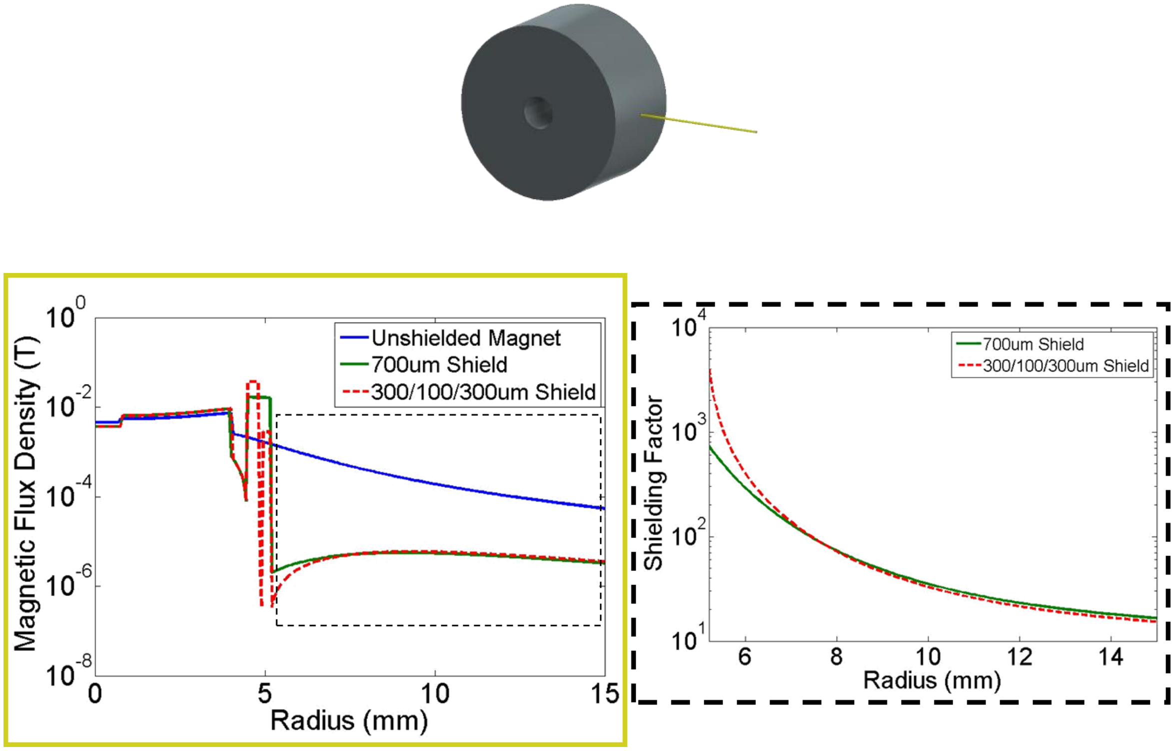

Figure 4.9: Transverse cutline (yellow) of the simulation in Figure 4.8 comparing a 700 µm shield to an equivalently thick two layer shield with 300 µm layers. Flux density for outside the magnet is shown (black dotted) indicating decreasing shielding factor with distance away from the magnet.

However, a reduction in on-axis field of the permanent magnet can be observed in the presence of the shields and requires further study. Figure 4.10 shows the results of on-axis flux density with and without the multilayer shield. The optical isolators utilize precise Faraday rotation of the incoming light polarization with the magnetic field. Thus, significantly altering the field inside the crystal can render the device useless. Based on simulation, the presence of the shield causes a 20% difference in the magnetic flux density. It is therefore critical to electroplate consistent material to create reproducible shifts that can be compensated for in system design.

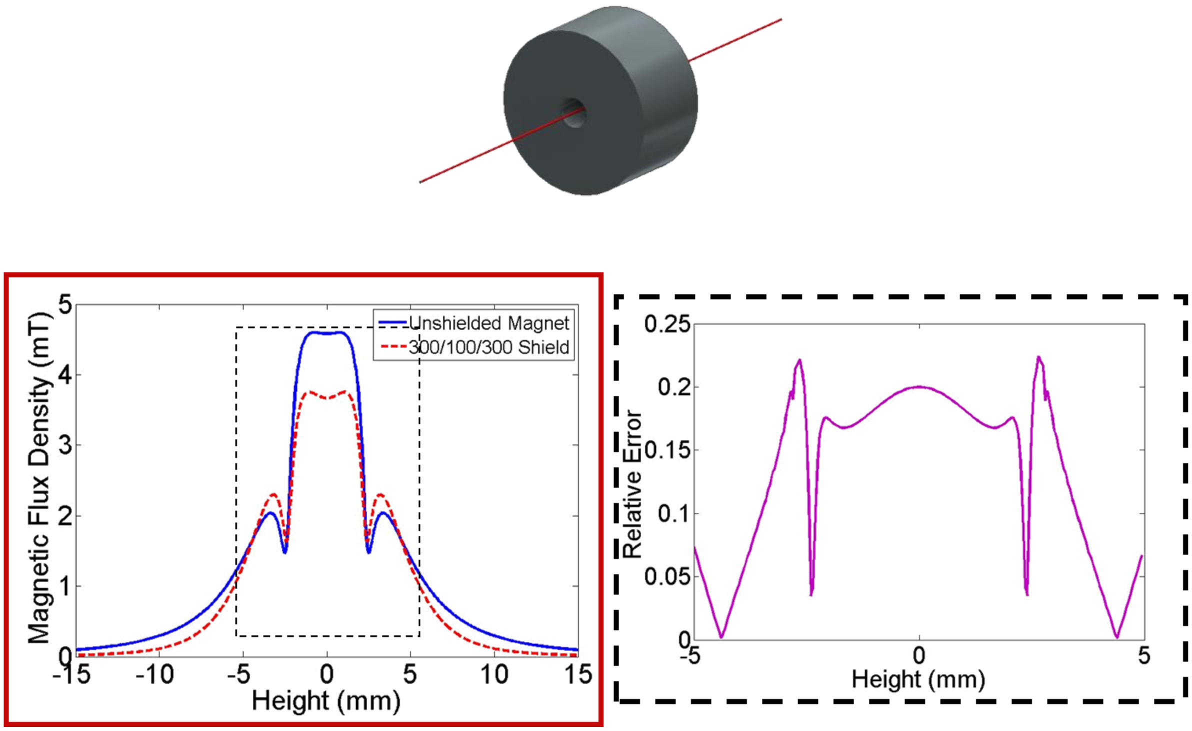

Figure 4.10: Longitudinal cutline (red) of the simulation in Figure 4.8 comparing the on-axis field from the unshielded magnet to a two-layer shield. The flux density is shown to drop slightly in the center with the shield, thereby necessitating compensation.

Chapter 5: Fabrication

Section 5.1: Millimeter-Scale Shield Fabrication

While electroplated shielding layers can offer unmatched shielding factors for shields with sub-millimeter lengths, it is difficult to characterize their shielding factor with available equipment. Thus, a process was designed to demonstrate and verify permalloy shielding factors at the millimeter scale where gaussmeters or Hall effect probes could be inserted within the shields with an externally applied field.

Section 5.1.1: 3D Printed Cylindrical Molds

While intended for packaging AMO systems, the shielding fabrication process itself was first demonstrated on 3D printed molds which could ultimately encompass the devices to be shielded. Cylindrical molds with dimensions based on the simulations in Chapter 4 were designed using Autodesk Inventor. Additional wings were devised on the cylinders to allow for sputtering stability and electroplating contact in the subsequent fabrication steps. Molds were printed with Stratasys Objet24 PolyJet and a Solidscape 3Z PRO printers. Both are inkjet-style printers capable of using sacrificial material to print overhanging structures. The Objet24 uses a proprietary ultraviolet-curable polymer while the 3Z PRO prints with heated, structural wax. Figure 5.1 shows two cylinders printed with each prototyping tool. While the Objet24 provides a strong base for the subsequent steps, the model material is difficult to remove and thus needs to be printed hollow to allow insertion of a magnetometer. On the other hand, the 3Z PRO parts are more fragile but can be dissolved away once the shield is deposited, yielding a smaller shield for the same cylinder diameter as printed. Shield dimensions were iterated based on the minimum resolution achievable by each printer, ultimately resulting in cylindrical molds ranging from 3 mm to 6.5 mm outer diameter.

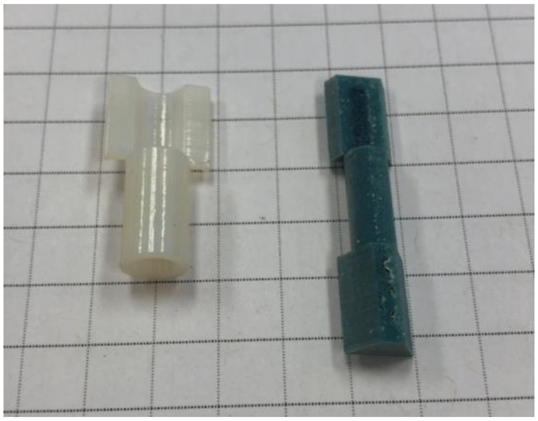

Figure 5.1: 3D-printed polymer mold using the Objet24 (left) and 3Z Pro (right). Grid spacing is 0.25 inches.

Section 5.1.2: Seed Layer Deposition

In order for permalloy to be electrodeposited, the mold must have a conductive surface through which electrons can travel. Thus, an electroforming seed was deposited on the molds by DC magnetron sputtering (Denton Discovery). The seed layer consisted of 300 nm Cu to carry the electroplating current and 50 nm Ti as a cap to prevent oxidation during transfer. Cylinder molds were taped to stand upright on the rotating chuck in the vacuum chamber as shown in Figure 5.2, allowing the sputtered metal to uniformly deposit on all sides. Kapton tape occluded the holes of the hollow cylinders to prevent permalloy from eventually electroplating unevenly on the inside walls. For cylinders printed with the 3Z PRO, vacuum pressures during metallization were increased to prevent the sample from outgassing during sputtering.

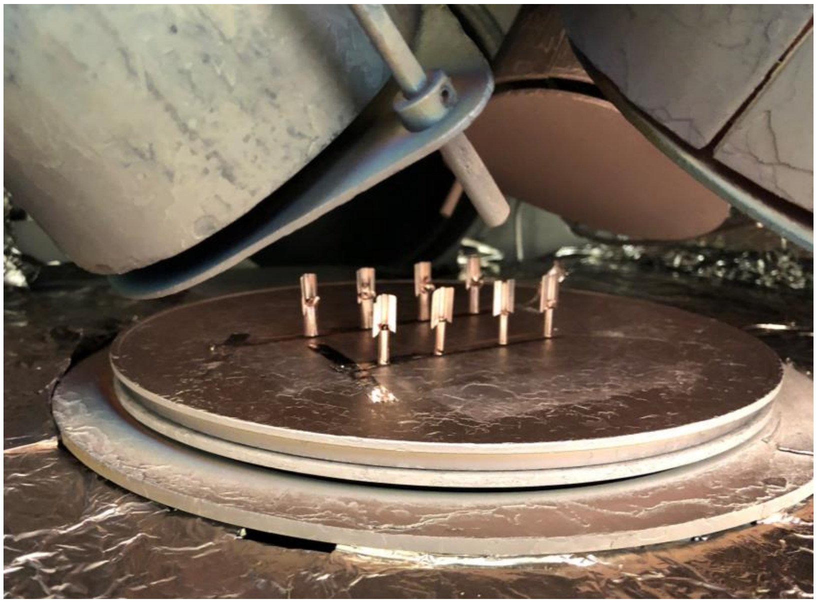

Figure 5.2: Picture depicting the 3D printed cylinders in the sputtering chamber coated with copper.

Section 5.1.3: Permalloy Electrodeposition

The process of plating permalloy in the specific 80% nickel, 20% iron ratio is challenging. The codeposition of the alloy must be done at a precise ratio, as moderate changes in the alloy composition lead to deviations in permeability, saturation, and coercivity. Exposure to oxygen during deposition can form insoluble iron-oxide compounds which contaminate the material, altering the composition. Insufficient agitation also leads to the formation of hydrogen bubbles which create voids in the deposited film. In this work, the shielding deposition process was modified from the permalloy electroplating process detailed by Glickman et al., as shown in Figure 5.3 [31]. This method has previously demonstrated electrodeposited permalloy with high permeability and saturation by minimizing bath exposure to oxygen and agitating the wafer inside the Nernst diffusion layer. This is accomplished by plating in a nitrogen-purged atmosphere, sealing the anode behind a porous membrane, and using parallel agitation fins less than 500 µm away from the wafer surface.

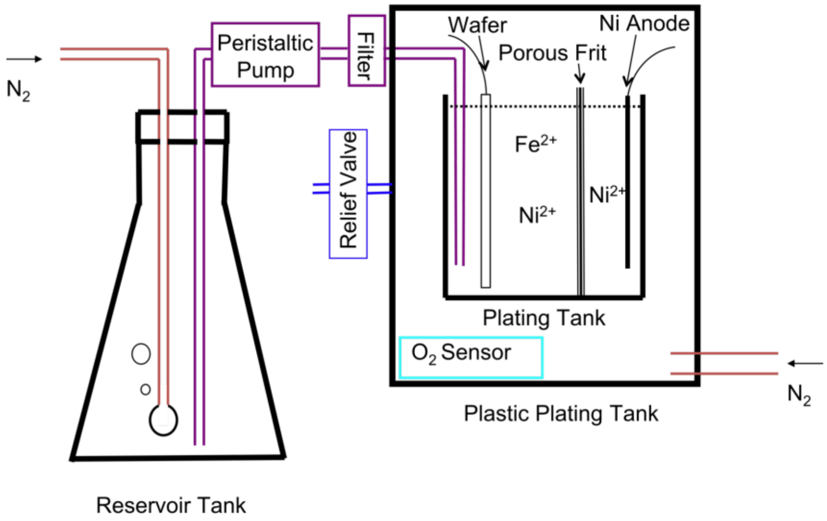

Figure 5.3: Illustration of the UCLA permalloy plating process. The bath is kept in an inert nitrogen atmosphere to prevent iron oxide particles from forming. A porous frit isolates the anode from the plating bath to prevent anode contamination, and a filter catches any undesired particles each time the bath is pumped to the reservoir tank [31].

In the shield deposition process, a piece of copper tape was attached to the wing of the shielding mold to electrically connect the seed layer. A chemically resistant tape was used to seal the copper tape and the remainder of the wings, leaving an opening for a plating contact. Immediately prior to electrodeposition, the exposed Ti was etched off in 1% hydrofluoric acid (HF) to expose the copper seed underneath. The mold was then taped to the custom plating fixture in Figure 5.4 and immersed in the pH-balanced plating bath. The modified fixture was designed in Autodesk Inventor and printed with the Objet 24. It was attached onto an existing agitation scheme used for electrodeposition on a silicon wafer. Thus, the cylinder surface could be vigorously agitated on both surfaces during electroplating. The samples were plated at 100 – 150 A/m^2, resulting in a deposition rate of approximately 80 to 100 nm/min depending on the open area of the cylindrical mold. To maintain uniform electroplating conditions, the sample orientation was also rotated 180° halfway through deposition. However, as plating occurred with a single anode, the plating current density passing through the shield side facing the anode was higher than expected. Specifically, this effect was more noticeable on the backside of the shield which was plated facing the anode last. Upon completion, the sample was rinsed in deionized (DI) water and dried with a nitrogen gun. The results of the plating can be seen in Figure 5.5.

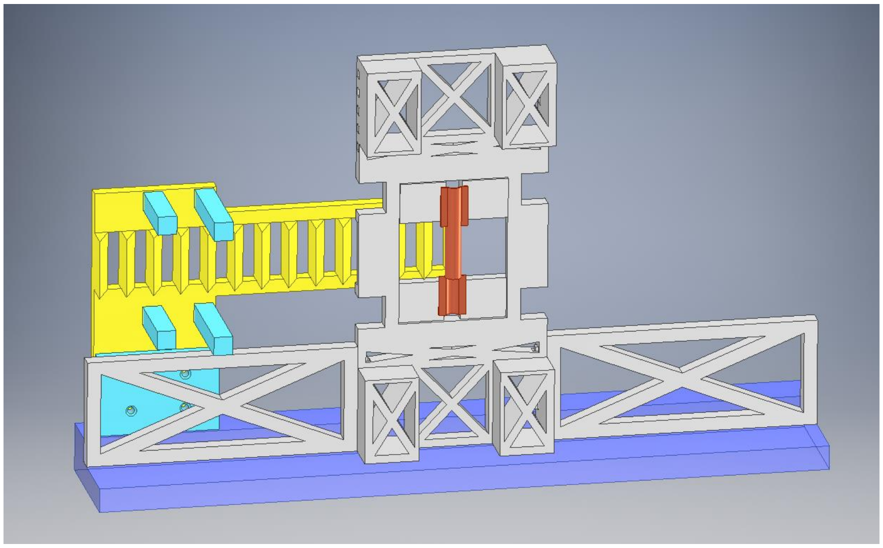

Figure 5.4: Illustration of the modified permalloy electroplating setup for the cylindrical mold (orange). The backside agitation fins (yellow) attach to the original plating fixtures.

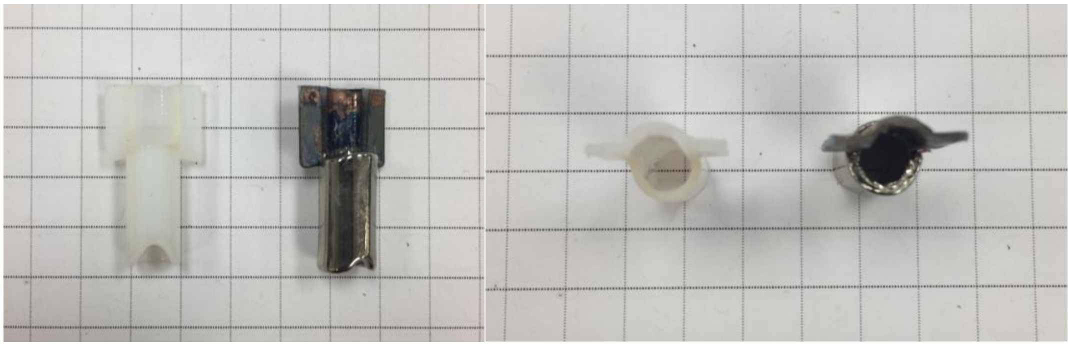

Figure 5.5: Photographs of the transverse view (left) and longitudinal view (right) of the unplated cylinder and 300 µm plated permalloy shield. Grid size is 0.25 inches.

Section 5.1.4: Double Anode Electrodeposition

While the modified process above was able to deposit acceptable permalloy for magnetic shielding, the sample rotation during electrodeposition reduced the scalability of the overall method and resulted in non-uniform material on the front and backside of the shield. The root cause is elucidated in Figure 5.6. The plating current on the power supply is set by the surface area of the plating mold and the desired plating current density, which affects material stoichiometry. In the single anode case, the shield side facing the anode ends up with a higher plating current density than expected as it provides a lower resistance. Subsequently, this also reduces the plating current density of material on the backside. However, if the sample could be simultaneously plated on both sides, the plating current density could be normalized along with the resistance from each anode to the mold surface.

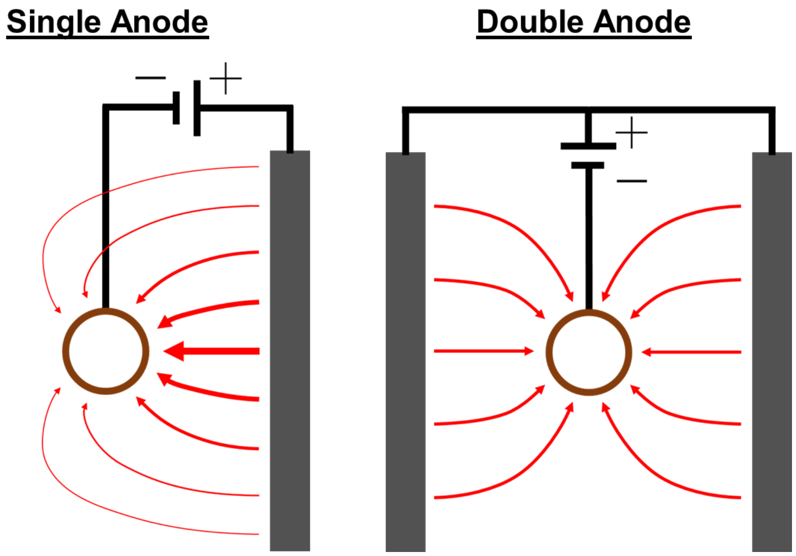

Figure 5.6: Diagram of the electroplating current density from anode to the sample for a single anode setup (left) and a double anode setup (right). Red arrows indicate the magnitude of plating current flowing from the anodes to cathodes.

Thus, to address this issue, further enhancement was made to the plating fixtures to allow electroplating with two anodes on opposing sides of the shielding molds as detailed in Figure 5.7. The new fixture was no longer compatible with the existing agitator and thus had too many components to be printed at once in the Objet 24. The design allowed for individual pieces to be printed and assembled to form the new agitation setup. The large pieces on either side of the sample holder allowed for an extra compartment for the second anode, enabling uniform current to flow and deposit onto both sides of the sample simultaneously. Furthermore, multiple parallel fins surrounded the sample during plating, again resulting in vigorous agitation for a smoother permalloy surface.

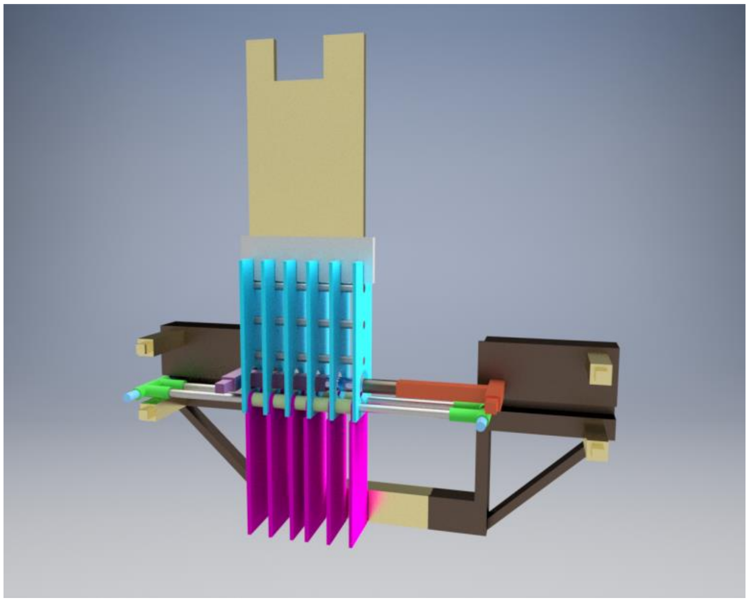

Figure 5.7: Illustration depicting half of the double anode plating fixture. The fins (cyan and magenta) agitate the entire bath, providing vigorous agitation of the shield mold held by the sample holder (orange). Agitation fins are locked in place with polypropylene rods connected to a holder (green).

Section 5.2: Sub-Millimeter-Scale Shielding Fabrication

As simulated in Chapter 4, optimal multilayer shielding factors are obtained by shrinking the characteristic lengths and heights of cylindrical shields to the sub-millimeter-scale. Furthermore, electrodeposition of permalloy and copper is sequentially compatible, allowing rapid laminations of thin shielding layers. Thus, a related process for batch fabrication of multilayer magnetic shielding was also demonstrated by incorporating microfabrication techniques, seen in Figure 5.8. The process consists of defining a pit in which to fit a shielded device, coating the pit with electroplated shielding layers, polishing the shielding layers to reveal the pit edges, and combining the pit with a mirrored half to form a completed shield. Shielding pits were designed with diameters varying from 1.5 mm to 6 mm and snaked interconnects to mitigate leaking of magnetic fields through the electrical interconnects.

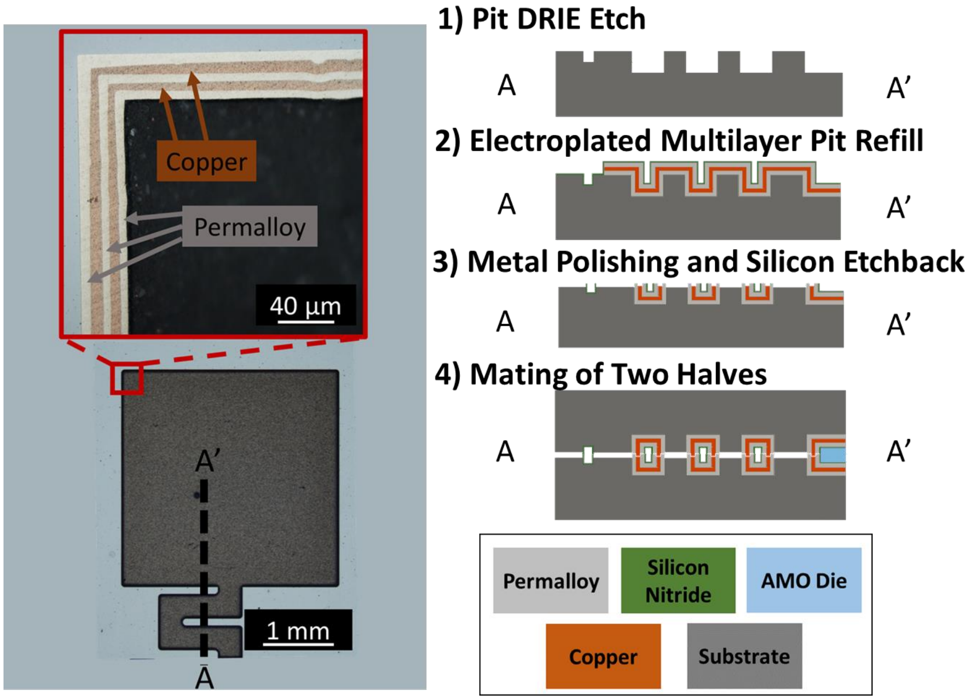

Figure 5.8: Microscope image of the sub-millimeter-scale shields (left) showing the plated multilayers (red) and illustration of the microfabrication process steps (right).

Section 5.2.1: Shielding Pits

A 2 µm oxide layer was deposited onto a 500 µm-thick silicon wafer to act as a hard mask for the subsequent etching steps using plasma enhanced chemical vapor deposition (STS Multiplex CVD). The shielding pit pattern was lithographically defined on a 3 µm-thick positive tone photoresist (SPR 220-7), where it was transferred to the oxide layer with a dry plasma etch (STS AOE). After stripping the photoresist off in acetone, a deep reactive ion etcher (Plasma-Therm DSE II) was used to create 235 µm deep pits in the silicon wafer. A microscope image of these pits is shown in Figure 5.9. Next, a 500 nm SiO_2 film was grown by thermal oxidation in a wet furnace (Mini 3600) to isolate the silicon from the subsequent metal layers. The wafer was then sputter-etched for 5 minutes with a DC bias, and an electroforming seed was deposited using radio frequency (RF) sputtering (CVC 601). An initial 30 nm of Ti provided adhesion to the substrate followed by the 300 nm copper for current carrying and a final 50 nm Ti oxidation cap.

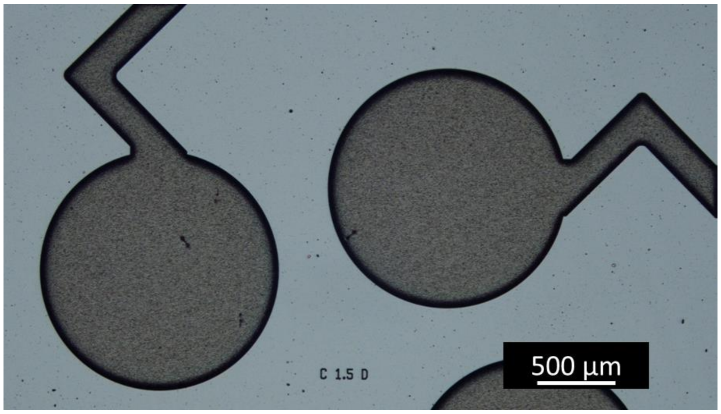

Figure 5.9: Microscope image of 1.5 mm diameter circular pits with a kinked interconnect.

Section 5.2.3: Multilayer Electrodeposition

Next, 50 µm of negative tone photoresist (KMPR 1025) was spun on the wafer and patterned to isolate individual dies for each shield. This prevented electroplating in the lanes between each die to alleviate dicing issues. Then, similarly to the millimeter-scale shield fabrication, a 1% HF etch removed the top Ti capping layer prior to electroplating. 10 µm of permalloy was deposited using the same plating fixtures as outlined by Glickman et al. for wafer-scale agitation at 50 A/m^2 [31]. Afterwards, another 1% HF dip removed native oxide, and a 10 µm Cu film was electroplated onto the wafer from a phosphorized copper anode in a commercially available sulfate-based solution (Technic Elevate 6320) at 50 A/m^2. The copper plating was done with custom 3D printed plating fixtures, and the anode was contained within a polypropylene mesh filter. The permalloy and Cu depositions were repeated until three 10 µm layers of permalloy and two 10 µm layers of Cu had been plated. Figure 5.10 shows the shielding pits after the 50 µm total shielding layers were deposited.

Figure 5.10: Microscope image of a 1 mm diameter and 2 mm diameter circular pit with 50 µm of permalloy and copper electroplated.

To electrically isolate the shields from the interconnects to be contained within them, a 1 µm insulating Si_3N_4 film was then deposited by PECVD (STS Multiplex CVD). The wafer was then polished to expose the shield edges via chemical mechanical polishing (Logitech CDP) with a 100 nm alumina slurry. The wafer was thoroughly cleaned using ultrasonic agitation in an acetone bath to remove any leftover polishing slurry and metallic debris. Figure 5.11 shows the exposed edge of the shield after polishing.

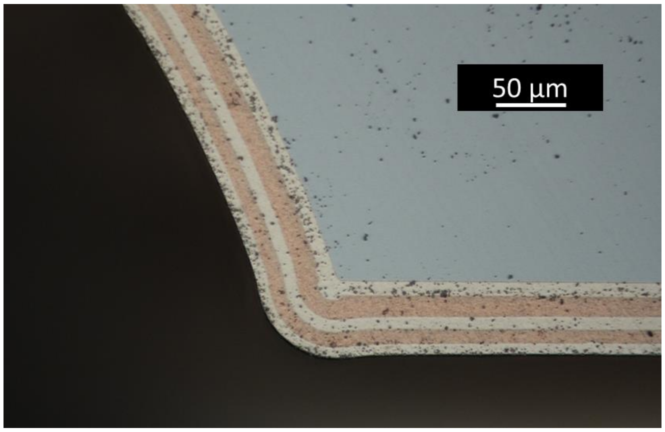

Figure 5.11: Microscope image of the multilayer electroplated edge of a shielding pit after chemical mechanical polishing.

Section 5.2.4: Alignment Structures and Shield Enclosure

In order to aid the alignment of halves of the shield, circular pits were etched into the silicon substrate along with the shield pits themselves. To create a shape to complement these alignment pits, 50 µm of structural photoresist (SU8 2000) was spun onto the wafers and patterned into circular pillars. The resulting film was annealed in vacuum for 8 hours at 200°C to harden the resist. Figure 5.12 shows the resulting alignment pits and pillars.

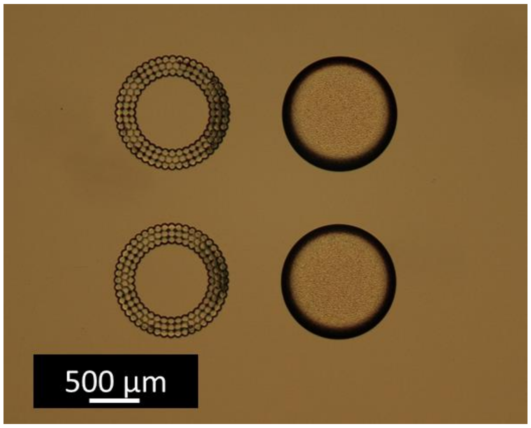

Figure 5.12: Microscope image of the 1 mm wide structural resist pillars (left) and silicon pits (right) for alignment of the shield halves.

At this point, the individual dies were singulated using a dicing saw along the lanes defined by the electroplating mold. To ensure a smooth surface finish, individual pieces were further polished (Logitech PM5) until the silicon surface was visible on all pieces. A brief isotropic chemical etch in XeF_2 gas raised the shield edges relative to the silicon surface. Each pattern on the die formed half a shield, and two shield halves were manually aligned to form a complete magnetic flux path. Alignment was aided by an infrared camera as seen in Figure 5.13 to see the metallic structures through the silicon backside. Once the edges were matched, a heated positive tone photoresist (SPR 220-3) was used as an epoxy to hold the shields in place.

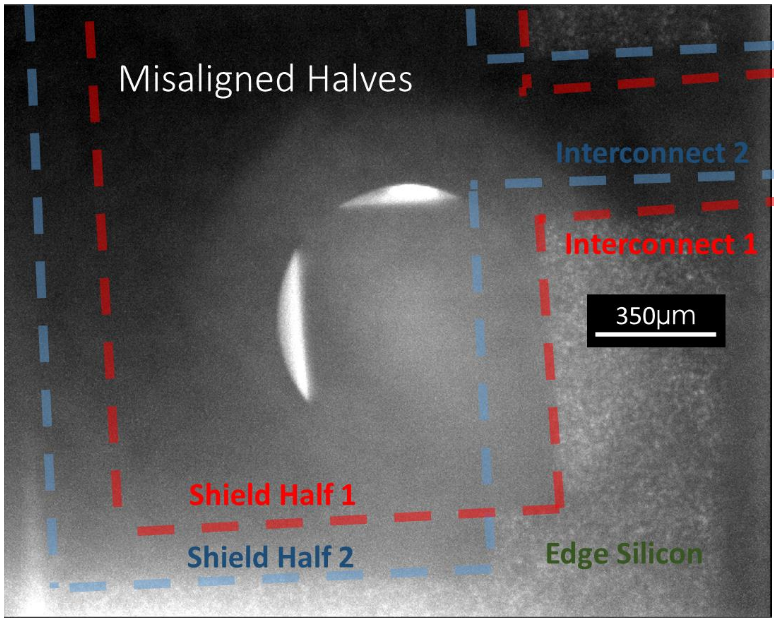

Figure 5.13: Microscope image taken with an infrared camera of two outlined shield halves (dotted red, dotted blue) for alignment.

Section 5.2.5: Printed Circuit Board Coils

Due to the difficulty of enclosing a sufficiently sensitive magnetometer within the sub-millimeter-scale shields, a flux source was instead inserted within the shields. The field was measured external to the device, as would occur if a field-generating component were being shielded. Inductive planar coils with less than 500 µm total thickness were fabricated on flexible printed circuit boards (FlexPCB) and placed inside the microfabricated shield halves. Coils were manufactured on both sides of the board substrate and connected in series at the center to maximize the amount of flux generated per unit area. Various interconnect shapes were also incorporated into the board cutouts to fit through the snaked shield pinholes. Figure 5.14 shows an example coil placed within the shield molds to be enclosed together.

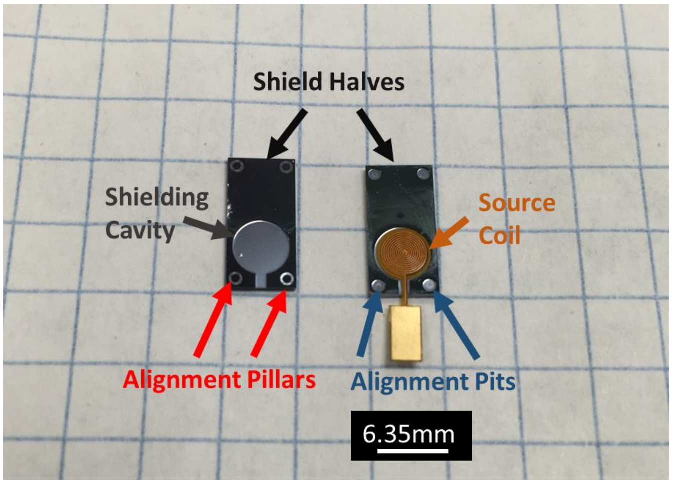

Figure 5.14: Photograph of two shield halves with alignment pillars (red) and alignment pits (blue) with the planar coil (orange).

Chapter 6: Characterization

Section 6.1: Millimeter-Scale Shielding Characterization

A diagram of the characterization scheme for the millimeter-scale shields is shown in Figure 6.1. A magnetic field was applied externally using an iron core electromagnet, which was placed in three concentric cylindrical mumetal shields to mitigate any magnetic noise. The applied flux densities were measured using two different Hall effect probes while the probe was inserted into an unplated dummy mold and the plated shield to be characterized. Photos of the actual measurement setup are shown in Figure 6.2.

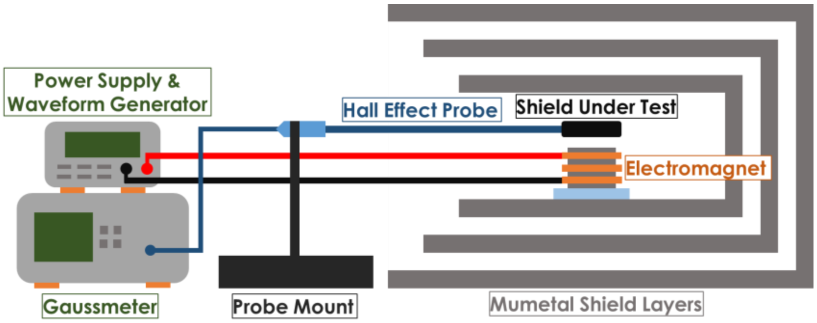

Figure 6.1: Illustration of the characterization setup used for the millimeter-scale shields.

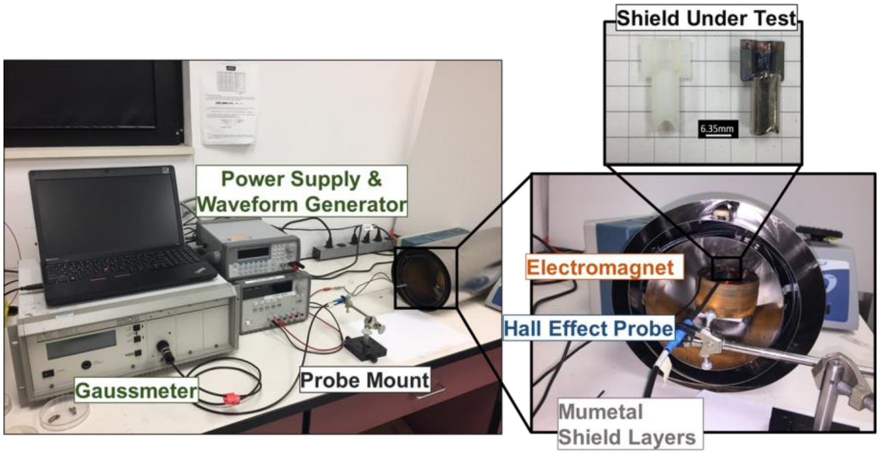

Figure 6.2: Photograph of the characterization setup of the millimeter-scale shields.

For larger shields, a transverse Hall effect probe (FW Bell HTF99-0608) was attached to a Gaussmeter (FW Bell Series 9900) for flux density measurement. A plot of magnetic flux density measured within the dummy and plated molds for a 6.5 mm single anode plated shield is shown in Figure 6.3. The maximum field achieved from the iron core at 1 A of applied current is nearly 40 mT. At around 0.5 A of applied current in the coil, corresponding to 19 mT of applied flux density, the shielded field quickly trends upwards, indicating material saturation. Afterwards, the shield redirects a constant 25 mT of flux density.

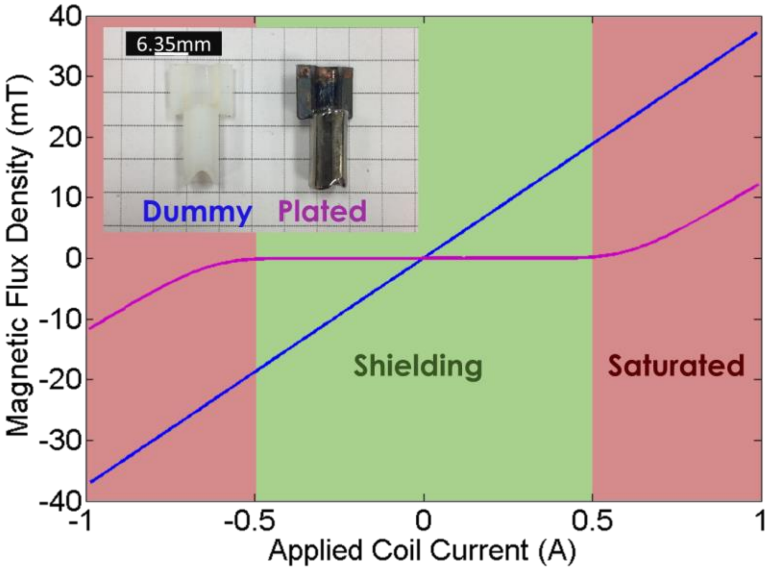

Figure 6.3: Plot of the flux density measured by the Gaussmeter probe to applied coil current for the dummy (blue) and plated (magenta) shields. Shielding effects are noticeably stronger in the low current (green) regime before the shields are saturated (red).

The Gaussmeter could be not be used to compare the shielding factor of various shields, however, as the probe had a width of 5 mm. Thus, a custom board was designed with a 2 mm width to interface with a chip-scale 3-Axis Hall effect magnetometer (AKM Semiconductor AK09918C), shown in Figure 6.4. As the board is more fragile than the probe, an extra 3D printed mount was attached to the sensor base to act as a support for the shields to be characterized. Due to the thickness of this extra layer, the Hall effect sensor was placed further away from the iron core tip and could not achieve as high of a magnetic flux density. Furthermore, this magnetometer saturated at 4.7 mT applied flux density, so unshielded fields needed to be characterized with the Gaussmeter instead.

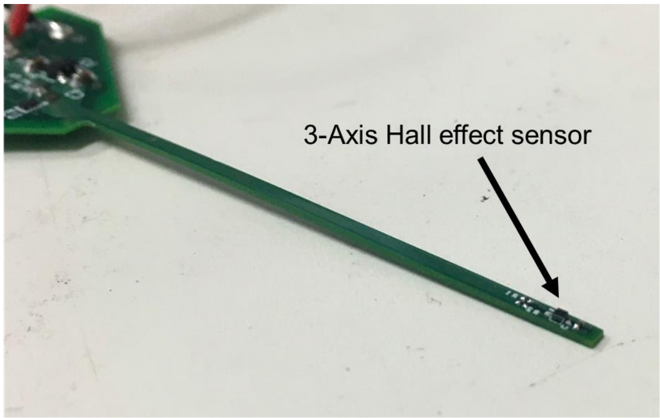

Figure 6.4: Photograph of the custom circuit board to interface with a chip-size magnetometer.

Section 6.1.1: Shielding Factor Measurements

Using the custom magnetometer, a 6.5 mm single anode plated shield and a 4 mm double anode plated shield were characterized by sweeping the coil current from -1 A to 1 A. The magnetic flux density parallel to the tip of the iron core was recorded at each step. The unshielded flux density was also recorded with the Gaussmeter in a separate sweep, and the transverse shielding factor was calculated as a ratio between the unshielded flux density and the magnetometer measurement with the shield in place.

Figure 6.5 shows the measured magnetic flux density from the magnetometer and transverse shielding factor for the aforementioned shields. Table 6.1 shows the measured maximum shielding factor for the two characterized shields. The shields were measured with both the front and back sides facing the iron pole to investigate the difference in shielding performance based on the two plating methods. The largest shielding factor of the four measurements was 257 at 7.9 mT of applied flux density for backside of the 6.5 mm shield.

It can be seen that as the applied field increases, the shielding factor trends downwards for all four shields due to the onset of magnetic material saturation. At high fields, the 4 mm shields outperform the 6.5 mm shields as expected based on shielding factor scaling. It is also evident that the shielding factor trends downwards at smaller applied flux densities. These curves were measured by sweeping the current from negative to positive values, with the zero crossing in measured flux density occurring before 0 A of applied current. Thus, at 0 A, the measured magnetic flux density is a positive value representing the remnant flux density of the magnetic shields. Since the field generated by the magnetic shield opposes the external field, the sign of the remanence is consistent with hysteretic behavior. When the coil current is instead swept from positive to negative values, the magnetic flux density at 0 A is negative, providing further evidence of remnant flux density in the shield. Thus, at low fields, shielding performance ends up being pinned by the remanence at 20 µT with the exception of the 6.5 mm backside which settles at 9 µT, resulting in the highest shielding factor.

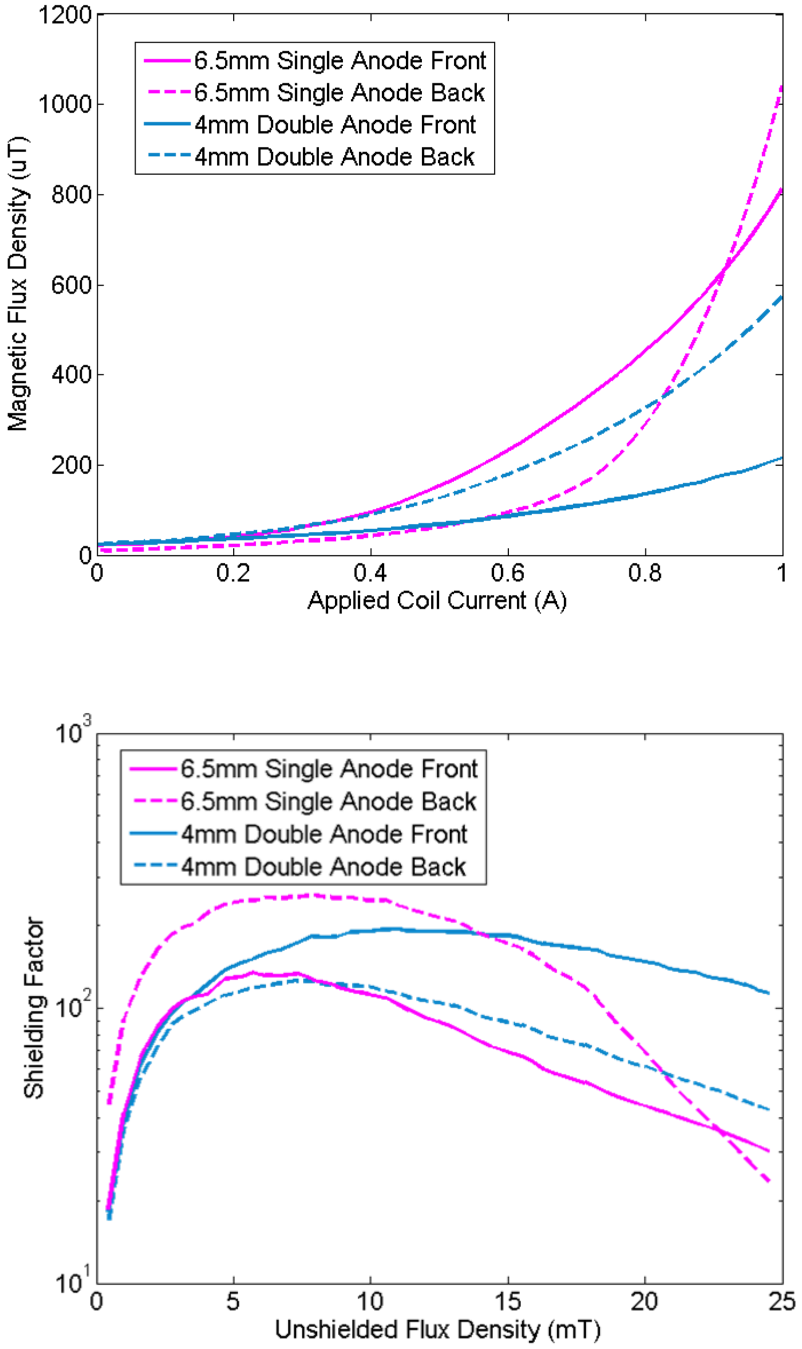

Figure 6.5: Plots of the measured magnetic flux density with the magnetometer to applied current (top) and calculated shielding factor to unshielded flux density (bottom) for 6.5 mm single anode plated (magenta) and 4 mm double anode plated (blue) shields. Measurements are done on the front-side (solid) and back-side (dotted) of the shields to compare uniformity.

Size [mm]	Anode	Orientation	Max Shielding Factor	Max SF Flux Density [mT]
6.5	Single	Front –	135	5.75
6.5	Single	Back --	257	7.90
4	Double	Front –	194	11.0
4	Double	Back --	126	7.31

Table 6.1: Comparison of the maximum shielding factor measured in Figure 6.5 and the applied flux density at which the maximum shielding factor was measured.

Section 6.1.2: Material Composition Comparison

To better characterize the difference in shield performance and verify the uniformity of the double anode electroplating, the material composition of the two samples was measured using energy dispersive x-ray spectroscopy (EDAX). The emitted x-ray counts are plotted in Figure 6.6 against the energy spectrum expected for nickel and iron, and Table 6.2 shows the measured iron concentration, the error from the expected 20% iron, and the difference between the front and backside of each sample. The currents given in the table are the plating current densities used to electroplate each sample. For the 6.5 mm shield, the shield front actually has relatively stoichiometric permalloy, but the backside, which was plated with a larger plating current density, has very low iron content. The iron content decreasing with increased current density has been reported extensively in literature for electrodeposited permalloy [48][49]. This also explains the decreased remanence of the shield as it consists of more nickel content. Meanwhile, the double anode material has slightly low iron content, but is very conformal in the deposited material composition. The slight discrepancy in the 4 mm mold uniformity is caused by the difference in resistance between the front and back anodes. For reference, another 4 mm diameter shield was plated at 100 A/m^2, and though the shielding factor could not be measured due to the shield splitting during plating, material composition was still measurable with EDAX. The material uniformity is slightly worse as the lower current likely magnified the difference in anode resistance.

However, the material had higher quality permalloy in terms of the nickel and iron content, implying the lower plating current density is closer to the ideal, stoichiometric operating point of the double anode permalloy plating bath. Ultimately, this work has demonstrated a novel double anode plating process to improve the uniformity of permalloy plated on a cylindrical mold, enabling batch fabricated, millimeter-scale magnetic shields for AMO components.

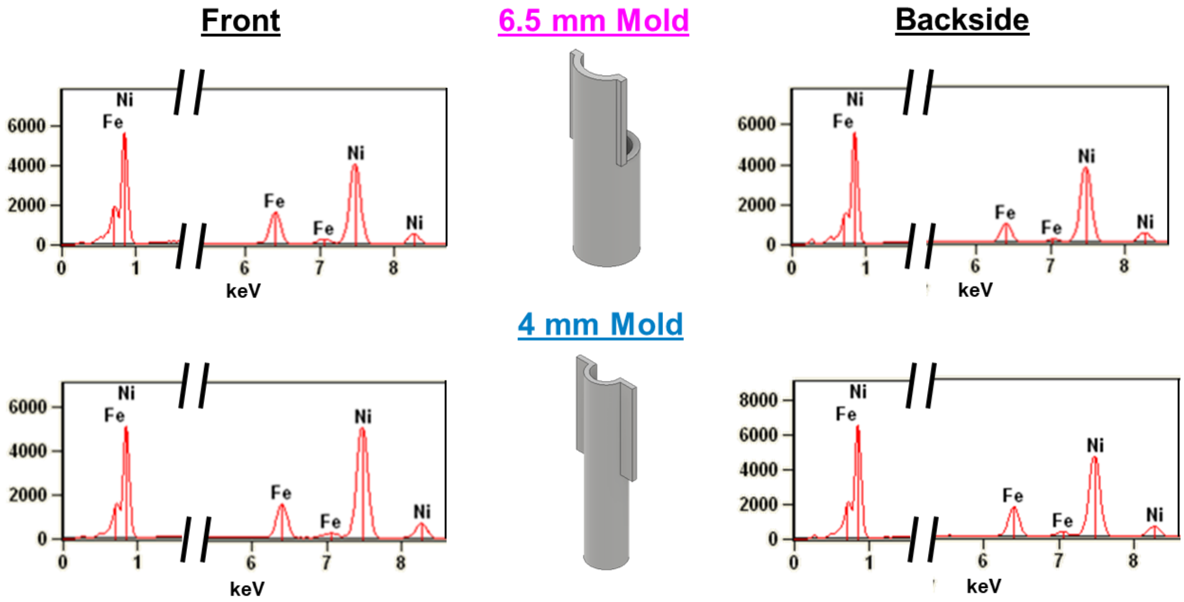

Figure 6.6: Plots of the measured x-ray counts from EDAX to the energy corresponding to nickel and iron for the 6.5 mm single anode plated shield (magenta) and 4 mm double anode plated shield (blue).

Size [mm]	Current [A/m^2] (S/D)	Front Fe [%] (Error)	Back Fe [%] (Error)	Difference [%]
6.5	150 (S)	18.34 (1.66)	11.26 (8.74)	7.08
4	150 (D)	14.57 (5.43)	16.52 (3.48)	1.95
4	100 (D)	17.43 (2.57)	21.82 (-1.82)	4.39

Table 6.2: Comparison of the measured iron content from EDAX for the 6.5 mm single anode plated shield (magenta), 4 mm double anode plated shield (blue), and 4 mm double anode plated shield at a lower current density (black).

Section 6.2: Sub-Millimeter-Scale Shielding Characterization

Characterization for the sub-millimeter-scale shields was performed using the inductive planar coils. The overall measurement scheme is outlined in Figure 6.7. As the dimensions of these shields were much smaller, the enclosed shields were epoxied onto 3D printed fixtures to help position and handle each test sample, as shown in Figure 6.8. The fixtures were inserted into a 3D printed mount which aligned their relative positions to the measurement equipment. The FlexPCB coils broke out to pads onto which connectors were soldered to power the coils through jumper cables. Finally, a longitudinal Hall effect probe (FW Bell SAF99-1808) and the assembled characterization setup were inserted into three concentric mumetal shields with Figure 6.9 depicting each step outlined above.

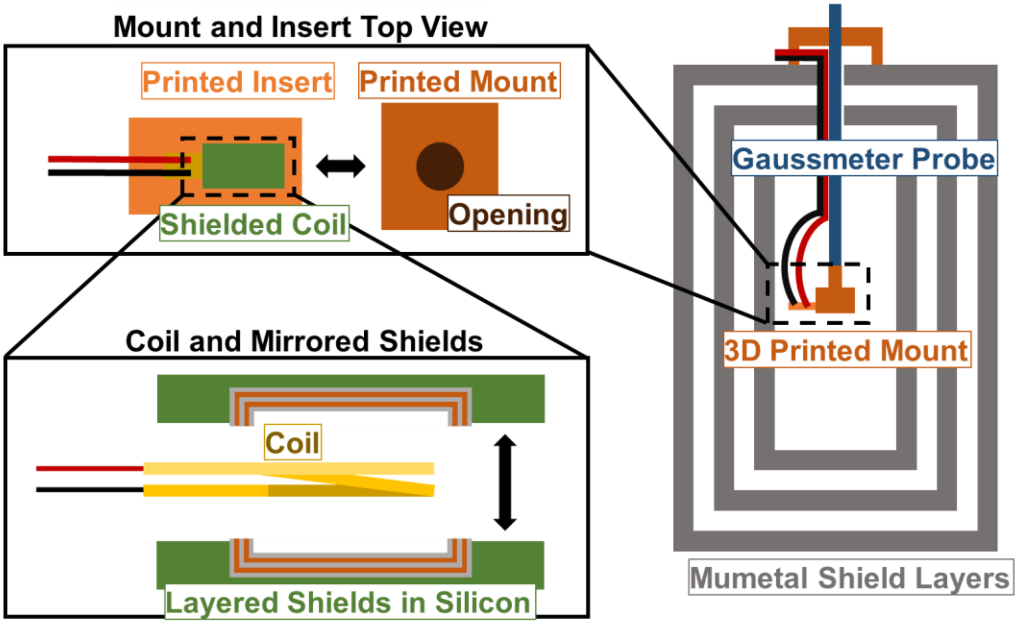

Figure 6.7: Illustration of the measurement setup used to characterize the sub-millimeter-scale shields.

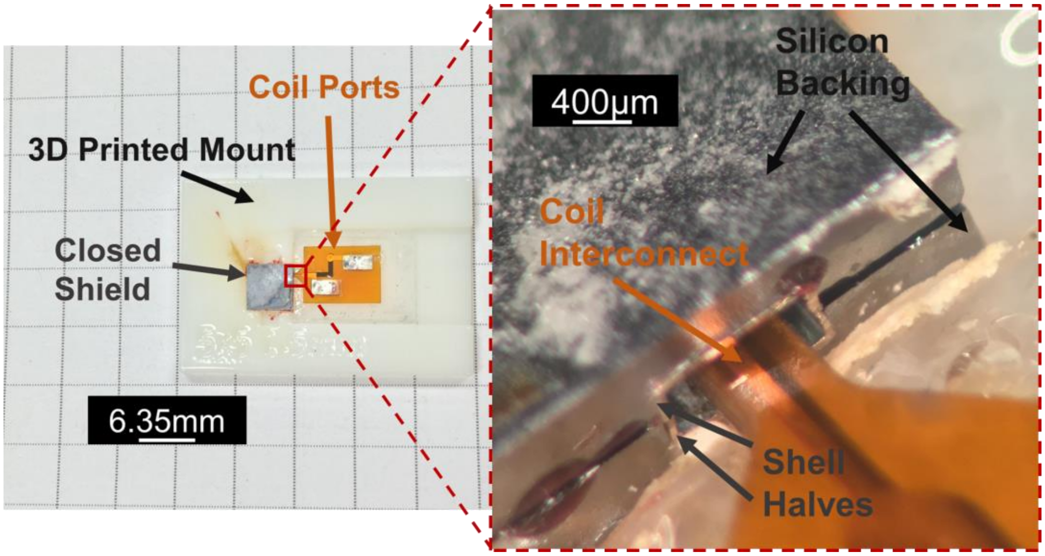

Figure 6.8: Photograph of the sub-millimeter-scale shields enclosed around a coil and mounted on a 3D printed slide (left) and stereoscope image of the interconnect to the enclosed coil (right).

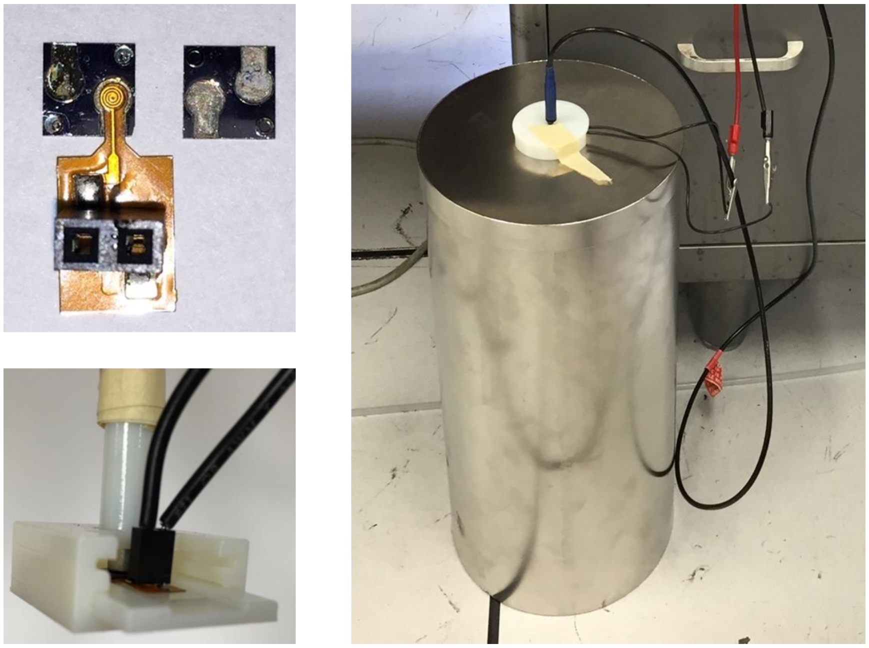

Figure 6.9: Photograph of the planar coil aligned to a shield half (top left) and 3D printed fixture inserted into the mount for measurement (bottom left). The mount is then placed within three mumetal shields for measurement (right).

Section 6.2.1: Shielding Factor Measurements

In order to calculate the longitudinal shielding factor of the sub-millimeter-scale shields, the current applied to the coils was swept from 0 to 500 mA to avoid burning out the relatively thin traces. The magnetic flux density generated was then measured at a fixed distance away from the coil while it was half encapsulated and fully encapsulated by the microfabricated shields. The longitudinal shielding factor was then calculated as the ratio of measured flux densities while accounting for the inductance variation measured using a precision impedance analyzer (Agilent 4294A).

Figure 6.10 shows the shielding factors measured from various microfabricated shields with the current applied to the inductive coils. Due to the thinness of the shields, the onset of saturation occurs faster and shielding factor is significantly smaller. However, consistent with analytical expressions, the shielding factor mostly improves for smaller versions of microfabricated shields as compared to larger ones due to geometrical factors and delayed saturation. Difficulty in alignment of the 10 µm shield edges resulted in variations of shielding factor measurements between samples. At 400 mA applied current, the shielding factor for a 3 mm shield varied from 3.5 to 14.3 depending on alignment. The highest measured shielding factor of 98 was measured for a 3 mm diameter shield at 55 µT applied internal field. This is the first ever shielding factor measurement demonstrated for sub-millimeter-scale electroplated magnetic shields.

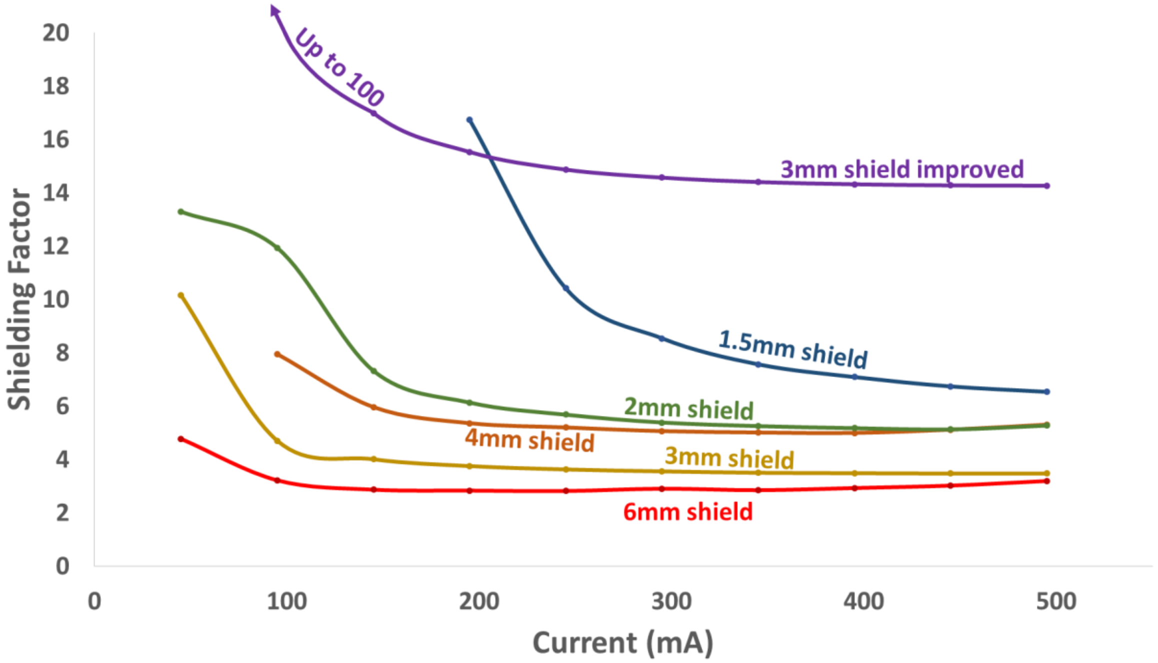

Figure 6.10: Plot of measured shielding factor to applied planar coil current for shields with 1.5 mm (blue), 2 mm (green), 3 mm (yellow), 4 mm (orange), and 6 mm (red) inner diameter. A 3 mm shield with improved alignment between the shield halves (purple) demonstrates nearly 100 shielding factor at lower applied currents.

Chapter 7: Future Work

Section 7.1: Millimeter-Scale Shields

To further improve on the work in millimeter-scale shields, the novel electroplating setup could be machined to be sturdier and more rigid during electroplating. Currently, due to the instability of the double anode plating setup, agitation within 500 µm of the plated sample is difficult, resulting in hydrogen bubble formation. This leads to a large internal stress buildup during deposition and pins the maximum film thickness achievable.

Characterization of these magnetic shields could be expanded on as well. Firstly, the iron pole tip and coil do not provide a uniform magnetic field over a large region and cannot achieve over 40 mT of magnetic flux density. Replacing the field source with larger and stronger Helmholtz coils would give a more complete view of the saturation characteristics and potential shielding capability of the samples. A high-resolution Hall effect probe capable of fitting a sub-millimeter form factor must also be investigated for accurate measurements of larger shielding factors.

Finally, the shields fabricated using the double anode plating process could be used to encapsulate magnetically sensitive AMO components to investigate their ability to isolate the systems from disruptive, external fields. This would require collaboration with the various companies developing optical isolators, magneto-optical traps, photomultiplier tubes, and other components necessary for chip-scale atomic clocks.

Section 7.2: Sub-Millimeter-Scale Shields

The sub-millimeter-scale shields could easily be improved on with a more robust bonding and alignment process. Automated alignment and bonding can be done with commercially available equipment, such as the Amicra Die Bonder, enabling 2.5 µm of positional accuracy using optical cameras. This would significantly improve upon the shielding factors of the microfabricated shields, potentially demonstrating unprecedented field isolation.

However, to characterize the shielding factors, alternative characterization schemes must also be investigated. Microfabrication of the characterization coils themselves could yield higher ranging measurements to demonstrate the shield capabilities. Furthermore, microfabricated fluxgate magnetometers are promising for achieving the necessary sub-millimeter-scale field measurements and picoTesla resolutions required to measure the shielding factors.

Section 7.3: Future Applications of Miniaturized Magnetic Shielding

In addition to the devices in AMO systems requiring magnetic field isolation, various applications have been identified that could greatly benefit from the magnetic shields presented in this work. The National Aeronautics and Space Administration (NASA) and the National Oceanic and Atmospheric Administration (NOAA) have deployed various satellites with magnetometers for geomagnetic field measurement [50]. These measurements allow NOAA to detect sudden magnetic storms, which lead to potentially dangerous charged particle dynamics affecting spacecrafts or human spaceflight. The magnetometer for the Geostationary Operational Environmental Satellite – R Series is shown in Figure 7.1. In order to avoid noise from the satellite systems affecting the magnetic measurements, the fluxgate is mounted on an extended boom arm which must be deployed after the satellite has entered orbit. With the emerging interest of micro- and nanosatellites, the magnetic cleanliness of these tightly packed subsystems must be closely observed and can be readily addressed with the use of electroplated magnetic shielding where appropriate [51].

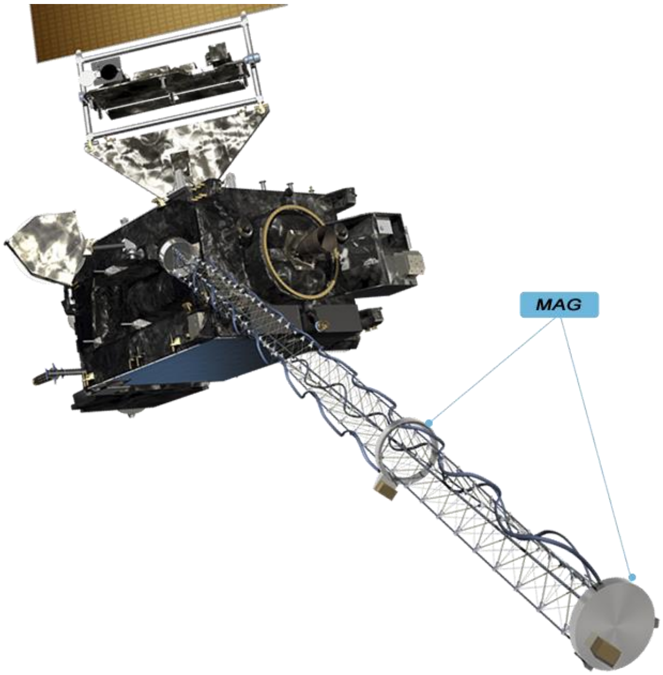

Figure 7.1: Diagram of a GOES-R Series satellite deployed by NOAA. A large boom arm is extended away from the main satellite body to minimize interference with the sensitive magnetometer measurements [50].

Furthermore, recent interest has developed in cryogenic optoelectronics, which takes advantage of photonic technologies to allow data transfer and communication with superconducting devices at over 10 Gpbs [52]. These systems can allow high clock rates for fast data throughput, but cryogenic requirements prevent the use of standard electrical interconnects which introduce parasitic heat loads. Thus, optoelectronic interconnects are necessary to achieve the desired data rates without compromising the performance of the system. Figure 7.2 depicts a suspended waveguide structure which could be used for out-of-plane optical coupling to the optical fibers [53]. These delicate interconnects are micromachined with bulk silicon techniques for fabricating Si/SiO_2 cantilevers. Integration of these rigid and fragile fibers with the magnetic shielding required for cryogenic devices proves to be difficult, but electroplated shielding could provide a path to compatible packaging of these two technologies.

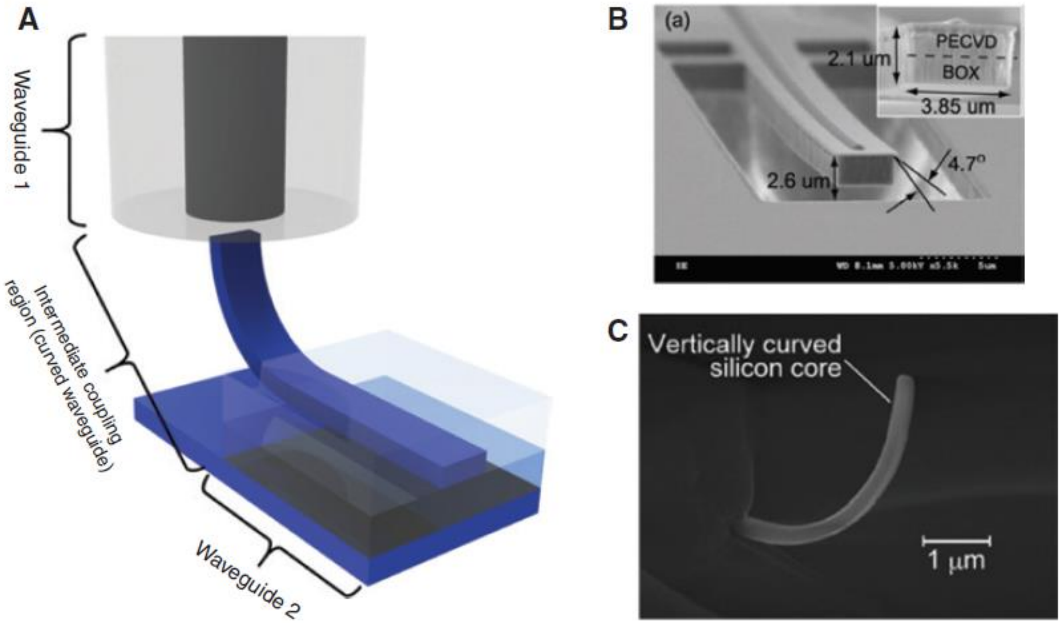

Figure 7.2: (A) Diagram of a vertically curved optoelectronic interconnect. (B) Scanning electron microscope image of a fabricated interconnect using thermal annealing techniques. (C) Scanning electron microscope image of a fabricated interconnect using ion implantation techniques. [53]

Chapter 8: Conclusion

Overall, this work has demonstrated a novel plating process for conformal permalloy deposition around millimeter-scale devices. The maximum achieved shielding factor was 257 for a 6.5 mm diameter, 300 µm thick permalloy shield. Furthermore, a 3 mm diameter, 50 µm thick multilayer shield achieved a shielding factor of 98. This is the first ever measurement of a shield in the sub-millimeter regime. Fabricated using a novel microfabrication process, it demonstrates a promising path towards high performance multilayer shields for even smaller sub-millimeter packages. The flexibility in shield thickness and shape design, ease of component integration, and scalability through batch fabrication can enable compact integration of magnetic devices for AMO microsystems and other magnetic microelectronics where the constant trend of miniaturization brings magnetically sensitive components closer together.

Appendix A

Section A.1: Alternative Interpretation of Magnetic Shielding

While low frequency magnetic shielding can be considered as providing a low reluctance path to redirect fields away from a protected area, field suppression can also be interpreted using the concept of material magnetization. This concept is illustrated in Figure A.1. As an external field is applied to a material, the magnetic spin moments and domains within align, forming an internal magnetization. However, the alignment then produces its own magnetic field, which follows the external field within the material, but opposes it outside. Thus, in the regions near the magnetized material, the external magnetic field is suppressed, effectively shielding the field.

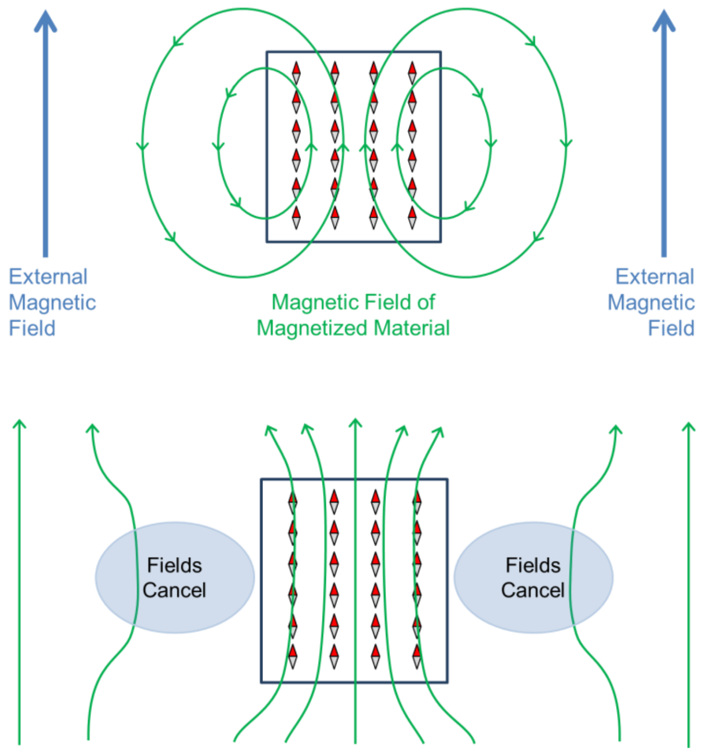

Figure A.1: Diagram of the magnetic flux density created by an externally applied magnetic field on a magnetizable material (top) and the superposition of the external field and field from magnetized material (bottom).

Section A.2: Alternative Interpretation of Multilayer Shielding

With the aforementioned perspective of magnetic field reduction, an alternative approach to understanding multilayer shielding can also be considered. This is depicted in Figure A.2. A solid piece of magnetizable material is divided into three regions: green, red, and blue. The colored arrows correspond to the magnetic field produced by each region opposing the external magnetic field. The green region contributes to the most to shielding as it is closest to the shielded region in the center. It can be seen that the magnetic field in the red region actually reduces the magnetization of the green and blue regions, thereby lowering their effectiveness at suppressing the external magnetic field. Thus, by removing the material within the red region with an air gap or a unity permeability material, the red opposing field can be eliminated. This allows the blue and green regions to be further magnetized than with the presence of the red region, improving the shielding performance of the material. This effectively explains the benefit of multilayer shielding over a single layer shield with the same total thickness.

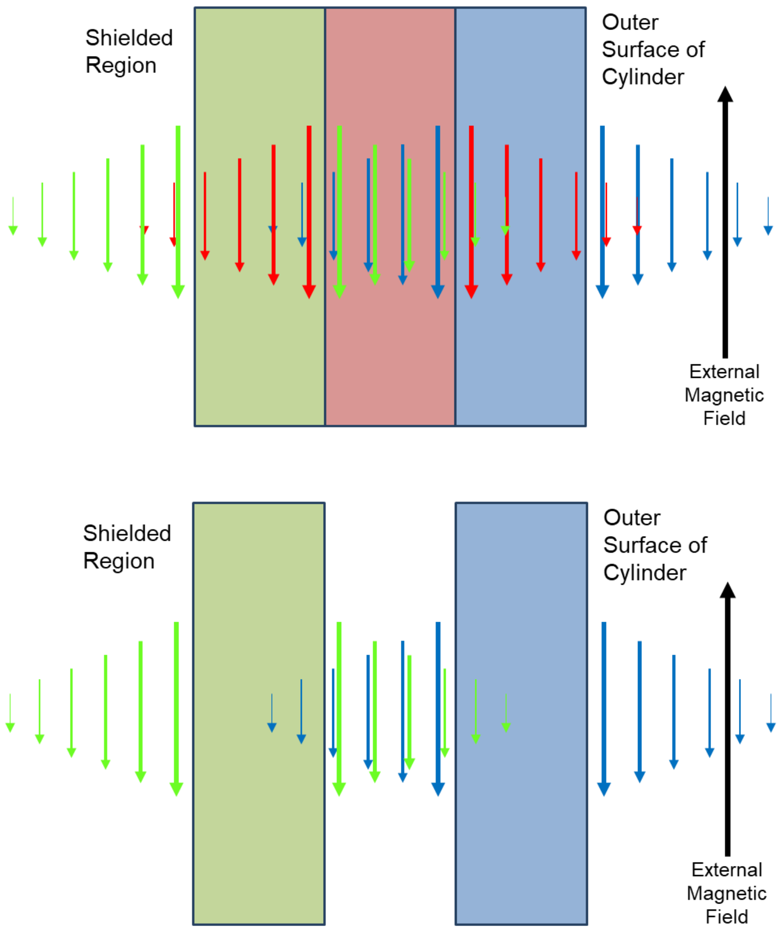

Figure A.2: Diagram of the magnetic flux density generated by the magnetized green, red, and blue regions of a single piece of magnetized material opposing an external magnetic field (top). Removal of the center red region also removes the corresponding red flux density opposing the magnetization of the green and blue regions (bottom).

References

[1] C. C. Finlay *et al.*, “International Geomagnetic Reference Field: the eleventh generation,” *Geophys. J. Int*, vol. 183, pp. 1216–1230, 2010.

[2] “The Truth About Magnetism And Watches | Quill & Pad.” [Online]. Available: https://quillandpad.com/2018/03/02/truth-magnetism-watches/. [Accessed: 06-Mar-2020].

[3] C. Y. Wang *et al.*, “Impact of external magnetic field on embedded perpendicular STT-MRAM technology qualified for solder reflow,” in *Technical Digest - International Electron Devices Meeting, IEDM*, 2018, p. 21.1.1-21.1.4.

[4] C. P. Bidinosti and J. W. Martin, “Passive magnetic shielding in static gradient fields,” *AIP Adv.*, vol. 4, no. 4, 2014.

[5] K. He *et al.*, “A high-performance compact magnetic shield for optically pumped magnetometer-based magnetoencephalography,” *Rev. Sci. Instrum.*, vol. 90, no. 6, 2019.

[6] “Le Système international d’unités (SI) The International System of Units (SI).”

[7] H. Lyons, “Atomic Clocks,” *Sci. Am.*, vol. 196, no. 2, pp. 71–82, Feb. 1957.

[8] J. Camparo, “The rubidium atomic clock and basic research,” *Phys. Today*, vol. 60, no. 11, pp. 33–39, Nov. 2007.

[9] D. B. Sullivan *et al.*, “Primary Atomic Frequency Standards at NIST,” *J. Res. Natl. Inst. Stand. Technol*, vol. 106, no. 1, pp. 47–63, 2001.

[10] A. Mann, “Amazingly precise optical atomic clocks are more than timekeepers.”

[11] W. F. McGrew *et al.*, “Atomic clock performance enabling geodesy below the centimetre level,” *Nature*, vol. 564, no. 7734, pp. 87–90, 2018.

[12] J. Müller *et al.*, “High Performance Clocks and Gravity Field Determination,” *Space Sci. Rev.*, vol. 214, no. 1, pp. 1–31, 2018.

[13] D. Calero, E. Fernandez, and M. E. Parés, “Positioning performance of chip-scale atomic clock GNSS augmentation systems,” *2016 8th ESA Work. Satell. Navig. Technol. Eur. Work. GNSS Signals Signal Process. NAVITEC 2016*, 2017.

[14] “Timing & Synchronization | Microsemi.” [Online]. Available: https://www.microsemi.com/product-directory/3425-timing-synchronization. [Accessed: 22-Mar-2020].

[15] R. Lutwak *et al.*, “The Chip-Scale Atomic Clock - Low-Power Physics Package,” in *36th Annual Precise Time and Time Interval (PTTI) Meeting*, 2004.

[16] D. M. P. Pozar, *Microwave Engineering*. John Wiley & Sons, 2009.

[17] T. Rikitake, *Magnetic and Electromagnetic Shielding*. Terra Scientific Publishing Company, 1987.

[18] A. J. Mager, “Magnetic Shields,” *IEEE Trans. Magn.*, vol. 6, no. 1, pp. 67–75, 1970.

[19] E. A. Donley, E. Hodby, L. Hollberg, and J. Kitching, “Demonstration of high-performance

compact magnetic shields for chip-scale atomic devices," *Rev. Sci. Instrum.*, vol. 78, no. 8, pp. 20–21, 2007.

[20] V. Kelhä, R. Peltonen, and B. Rantala, "The Effect of Shaking on Magnetic Shields," *IEEE Trans. Magn.*, vol. MAG-16, no. 4, pp. 575–578, 1980.

[21] T. J. Sumner, J. M. Pendlebury, and K. F. Smith, "Conventional magnetic shielding," *J. Phys. D. Appl. Phys.*, vol. 20, no. 9, pp. 1095–1101, 1987.

[22] D. Dubbers, "Simple formula for multiple mu-metal shields," *Nucl. Inst. Methods Phys. Res. A*, vol. 243, no. 2–3, pp. 511–517, Mar. 1986.

[23] R. C. O'Handley, *Modern Magnetic Materials*. John Wiley & Sons, 2000.

[24] D. Jiles, *Introduction to Magnetism and Magnetic Materials*, 3e ed. CRC Press, 1998.

[25] "Welcome to Metglas - Home of the Metglas Brazing Foil." [Online]. Available: https://metglas.com/. [Accessed: 06-Mar-2020].

[26] F. E. Luborsky, J. J. Becker, and R. O. McCary, "Magnetic Annealing of Amorphous Alloys," *IEEE Trans. Magn.*, vol. 11, no. 6, pp. 1644–1649, 1975.

[27] B. Li, L. Zhang, W. Fu, and H. Xu, "General Investigations on Manufacturing Quality of Permalloy via Selective Laser Melting for 3D Printing of Customized Magnetic Shields," *JOM*, pp. 1–11, Jan. 2020.

[28] J. H. Park *et al.*, "Electromagnetic interference shielding effectiveness of sputtered NiFe/Cu multi-layer thin film at high frequencies," *Thin Solid Films*, vol. 677, no. March, pp. 130–136, 2019.

[29] P. Arpaia, A. Ballarino, G. Giunchi, and G. Montenero, "MgB2 cylindrical superconducting shielding for cryogenic measurement applications: A case study on DC current transformers," *J. Instrum.*, vol. 9, no. 4, 2014.

[30] K. Song *et al.*, "Measurement, Simulation and Mathematical Estimation of Magnetic Field Shielding Effectiveness of Sputtered Shielding Materials using Spiral Coils," *2018 IEEE Symp. Electromagn. Compat. Signal Integr. Power Integrity, EMC, SI PI 2018*, pp. 47–51, 2018.

[31] M. Glickman, T. Niblock, J. Harrison, I. B. Goldberg, P. Tseng, and J. W. Judy, "High permeability permalloy for MEMS," *Tech. Dig. - Solid-State Sensors, Actuators, Microsystems Work.*, no. Table 1, pp. 328–331, 2010.

[32] T. Saito, "Open-type magnetic shielding method," *Int. J. Appl. Electromagn. Mech.*, vol. 33, no. 3–4, pp. 891–899, 2010.

[33] W. Esmarch, "Experimentelle Untersuchung der magnetischen Schirmwirkung multilamellarer Zylinderpanzer," *Ann. Phys.*, vol. 344, no. 16, pp. 1540–1552, Jan. 1912.

[34] I. Altarev *et al.*, "A large-scale magnetic shield with 106 damping at millihertz frequencies," *J. Appl. Phys.*, vol. 117, no. 18, 2015.

[35] M. Cheung, "Zero Magnetic Field Environment for EDM Measurement," 2003.

[36] L. Xuan, H. Dong, and C. Zhuo, "Compact multi-layer magnetic shields for chip-scale atomic devices," *8th Annu. IEEE Int. Conf. Nano/Micro Eng. Mol. Syst. IEEE NEMS 2013*, vol. 1, pp. 649–652, 2013.

[37] H. G. Hong *et al.*, “A Compact Physics Package of a Chip-Scale Atomic Clock with a Built-in Magnetic Shield,” *2019 Conf. Lasers Electro-Optics, CLEO 2019 - Proc.*, vol. 1, no. c, pp. 3–4, 2019.

[38] V. V. Dmitrenko *et al.*, “Electromagnetic shields based on multilayer film structures,” *Bull. Lebedev Phys. Inst.*, vol. 42, no. 2, pp. 43–47, 2015.

[39] S. Malkowski *et al.*, “Technique for high axial shielding factor performance of large-scale, thin, open-ended, cylindrical Metglas magnetic shields,” *Rev. Sci. Instrum.*, vol. 82, no. 7, 2011.

[40] S. Malkowski *et al.*, “Overlap technique for end-cap seals on cylindrical magnetic shields,” *IEEE Trans. Magn.*, vol. 49, no. 1, pp. 651–653, 2013.

[41] T. Saito, “Magnetic shielding effect from multiple configurations of open-type magnetic shielding walls compared to solid plates,” *J. Magn. Magn. Mater.*, vol. 322, no. 9–12, pp. 1540–1543, 2010.

[42] L. W. Hart and P. S. Greifinger, “Shielding of ELF Magnetic-Dipole Fields by Ferromagnetic Cylindrical Shells,” *IEEE Trans. Electromagn. Compat.*, vol. EMC-23, no. 1, pp. 2–12, 1981.

[43] S. M. Freake and T. L. Thorp, “Shielding of low magnetic fields with multiple cylindrical shells,” *Rev. Sci. Instrum.*, vol. 42, no. 10, pp. 1411–1413, 1971.

[44] I. Sasada, E. Paperno, and H. Koide, “Design of a large-scale vertical open-structure cylindrical shield employing magnetic shaking,” *J. Appl. Phys.*, vol. 87, no. 9, pp. 5962–5964, 2000.

[45] L. Gozzelino, A. Agostino, R. Gerbaldo, G. Ghigo, and F. Laviano, “Magnetic shielding efficiency of superconducting/ferromagnetic systems,” *Supercond. Sci. Technol.*, vol. 25, no. 11, 2012.

[46] C. I. Knudsok and J. R. Kench, “Annealing Effects in Plated-Wire Memory Elements, Part I: Interdiffusion of Copper and Permalloy,” *IEEE Trans. Magn.*, vol. 7, no. 4, pp. 852–858, 1971.

[47] S. R. Green, R. Malhotra, and Y. B. Gianchandani, “Sub-torr chip-scale sputter-ion pump based on a penning cell array architecture,” *J. Microelectromechanical Syst.*, vol. 22, no. 2, pp. 309–317, 2013.

[48] J. M. Quemper *et al.*, “Permalloy electroplating through photoresist molds,” *Sensors Actuators, A Phys.*, vol. 74, no. 1, pp. 1–4, 1999.

[49] Y. hua Zhang, G. fu Ding, Y. li Cai, H. Wang, and B. Cai, “Electroplating of low stress permalloy for MEMS,” *Mater. Charact.*, vol. 57, no. 2, pp. 121–126, 2006.

[50] “MAG | GOES-R Series.” [Online]. Available: https://www.goes-r.gov/spacesegment/mag.html. [Accessed: 21-Mar-2020].

[51] S. M. Belyayev and F. L. Dudkin, “Minimization of nanosatellite low frequency magnetic fields,” *Rev. Sci. Instrum.*, vol. 87, no. 3, p. 034705, Mar. 2016.

[52] E. Bardalen, M. N. Akram, H. Malmbekk, and P. Ohlckers, “Review of Devices, Packaging, and Materials for Cryogenic Optoelectronics,” *J. Microelectron. Electron. Packag.*, vol. 12, no. 4, pp. 189–204, Oct. 2015.

[53] G. Son, S. Han, J. Park, K. Kwon, and K. Yu, “High-efficiency broadband light coupling

between optical fibers and photonic integrated circuits," *Nanophotonics*, vol. 7, no. 12. De Gruyter, pp. 1845–1864, 01-Dec-2018.